Hes SO VALAIS WALLIS

Domain Engineering Sciences
Rte du Rawyl 47
CH-1950 Sion 2
Phone +41 27 606 85 11
Fax +41 27 606 85 75
info@hevs.ch

www.hevs.ch

Degree Course Life Technologies

Option Biotechnology

Diploma 2007

Cédric–Alain Bürki

Mixing and gas transfer studies in orbital shaken cylindrical vessels

Professor Kurt Eyer

Expert Florian Wurm

Sion, 1 February 2008

Preface/acknowledgements

I take this opportunity to acknowledge the people whose support undeniably helped me during my studies and more specifically during the 20 weeks of my diploma work. Each have played a role, whether it be small or large, to each, I personally thank them from the bottom of my heart.

First in line is Prof. Florian Wurm who allowed me to do my work in his lab, the LBTC, at the EPFL. I must mention that my internship for admission to the Haute Ecole Valaisanne 3 and a half years ago was also performed at the LBTC and this was truly my first practical hands on experience in the field of research on biotechnology.

To his team, Dr Lucia Baldi-Unser, Dr David Hacker, Dr Miriam Adam and to his secretary Marie-France Divorne, for being always there to answer any questions and propose their views on the matter.

A real special thank-you to Dr Matthieu Stettler and Xiaowei Zhang whose work I closely followed. Their insight into orbital shaking was of excellent use.

To Dr Gernot John for his interest in pH optodes evolution in a shaken bioreactor, and to PreSens GmbH for allowing the use of their pH-1 mini optical sensor

To mention Dr Maria De Jesus of ExcellGene SA, for her answers regarding analysis of cell supernatant and to Dr Tibor Anderlei and Fridolin (Lin) Wirth of Kuhner AG for their answers to my questions rearding shaker mechanisms

For my HEVs third year proffessors Simon Crelier, Kurt Eyer, Sergio Schmidt, who fortified my understanding of Biotechnology.

To my parents for their support, and particularly to André and Françoise for their hospitality during my three years of studies in Sion.

To my sweetheart, Uschi Bokuz, for all her love and support I say to you with my best romainian accent: "te iubesc". And to her parents who are always smiling and full of goodness.

Many thanx to my brother sylvain, my aunts and uncles: Marlene, Josianne & Jacky, and Micheline

I won't forget you, LBTC colleagues: Sophie, Carine, Seb, Gaurav, Lucia, Sarah, Virginie, Fanny, Christophe, Vincent, Celine, Myriam, Stephanie; thanks for the morning breakfasts and fun times at the lab.

A special thankyou to Martin Jordan and Martin Bertschinger for getting me to continually ask questions and find the solutions to these.

Of course, I must still mention all the friends from the 2007 life technology diploma year and to all the other friends at the HESSO Valais/Wallis

Contents

Introduction

State of the art

In Biotechnology, the art of cultivating the living organisms is in ever needing ways to improve its production of higher valued products. To do this, scientists have analysed the input and output of the organisms keeping in mind the law of conservation of mass (*Lavoisier*) which states that no matter can be produced or destroyed, it is merely transformed from one state to another. Even though it is not possible to try and counter this law, it is possible to make this transformation either more effective and/or simply faster. Scientists have always been looking for ways to increase the surface area of the substrates and putting them in contact with the microorganisms so as to increase the speed at which it may be converted. In this way, it is the method and tools used that are the key to speeding up the process as well as the urge by companies to get a product out onto the market as soon as possible because time is money.

In this work, I have looked into the mixing effect of orbital shakers. Although they have been around for a couple of decades, they were and still are mainly used for simple microorganisms (bacteria and yeast) cultures. No great effort has been made to look into the detail of what is happening. The microorganisms grow to useful concentrations and the product needs then only be separated and purified. This was done at the lab scale and then transferred to stir tanks or other complete culture systems. The simple shaking method was immediately replaced by the "newer" systems when going into large scale. No second thought was given to see if shaking technology would also be a valid culture tool. The newer technologies took bacteria and yeast cells to far higher concentrations than that reached on the shakers at the lab scale. But now cell technology and the use of animal cells are proving to be difficult in applying the bacterial standards of bioreactors. The cells are far more fragile and don't appreciate the enormous power input of stir tanks. To observe the evolution of shakers, one should go back to the origin of biotechnology.

In the beginning, biotechnology was not known as such, but converting grape juice to wine or fermenting a hops brew to beer used biotechnology to achieve the beverages. Cultures of the previous year's fermentation were used to inoculate new fermentations. Bread needed yeast to rise and yoghurt and cheese need specific bacteria to convert the milk. Through the years, the secret became defined and gradually people new exactly how to achieve a perfect result at each batch. Mixing has always been an issue, in all these processes. From the baker who kneads his dough to the cheese maker who will continually stir his warm milk mixture, an effort is made to get a homogenous result. This is the objective of the mixing stage in any biotechnological process.

It may be necessary to describe the different techniques in mixing a mixture, and hundreds if not thousands of methods have been developed to achieve this homogenous mixture in a quicker and more intelligent way. Whether it be through the shape of the stirring paddles, the pumping of the liquid to cause a flow, the turning of the vessel, the repetitive actions all achieved a sufficiently homogenous mixture. The mixing art is always adapted to the mixture which may vary from a mixture as fluid as water to an extremely viscous dough. This brought about technology changes. Robots were developed to knead dough as the power needed was far superior to what a human could do especially with increasing quantities. Higher mixing speeds were used to quicken the homogenous achievement and better materials were used to increase the strength of these robots.

Cleaning became an issue with the understanding of microorganisms. And stronger regulations were instated to prevent sickness. This all had an effect on the mixing strategies. The use of the microorganisms being mainly for feeding the population, it became necessary to show that it was as safe as possible. The mid nineteen hundreds had the greatest evolutions in understanding microorganisms and this led to using them in treating the ever increasing number of illnesses. This understanding of microorganisms and it's application in healthcare increased the necessity to have a 100% safe product. Although no one will guarantee this 100% safe product, every method is now being looked at to attain this perfect result. This race to guarantee safe products is pushing all scientists to critically look at their methods of production. The sterility issue has come up again and what was considered as safe before is now being closely inspected. Autoclaves were and still are a wonderful tool in obtaining a microbe free environment. Killing all these nasty and possibly life threatening bacteria is considered achievable with an autoclave, but the 100% result is still not there. Even if the harmful microorganisms are killed, their left over bits and pieces may still be dangerous.

I have spoken mainly of microorganisms which does not include viruses or the newly discovered prions. It is becoming harder and harder to show that all these "things" are removed from the products. As long as technology cannot inspect every vial of product down to the atom scale and show that only the product is in the vial, society has to live with the "almost" 100% safe product.

An effort has been made to protect the product from exterior sources and this can be associated to doing the least number of invasive procedures on the product, going from its first stage of production (the raw materials) right through to its final packaging process. Single use materials are a way of reaching these non-invasive procedures. Carry your process in one time usage bags form the beginning to the end. Do not use a same object for the next batch. Prevent all invasive and unnecessary manipulations. This brings us back to the question of how do you change the raw materials to the end product. Heating and cooling can easily go through bags as plastics are conductive to a certain limit. In biotechnology, temperatures rarely go above 60°C. Gases can be filtered and injected into the mixture, as well as other reactants. But mixing still is a problem. This is where different methods are being look at to mix an internal solution from an external force. Stirred tank bioreactors need a rotor and paddle inside the liquid to transmit the mixing force. To transmit the force from the outside of the vessel to the inside, magnets can be used to induce the external rotation to the internal shaft and paddle. Such an example can be seen with the CellMaker PLUS™ or with the XDR™ single-use bioreactor

Figure 1: CellMaker PLUS™ built by Cellexus Biosystems

Figure 2: Xcellerex XDR™ diposable bioreactor

The Xcellerex example simply took a stir tank bioreactor and converted all the parts in contact with the microorganisms to disposable materials. Disposable sensors are a necessity as the stir tank bioreactors were designed to control the aspect of pH, O2, temperature using online PID electronics. Apart form the sensors, the transmission of the mixing force requires carefully designed plastics and/or metals with high precision characteristics to prevent energy loss through these parts, thus increasing the costs of the disposable bag.

This issue of precise and expensive disposable parts is replaced in shaker technology by using gravity and centrifugal forces as the mixing energy. Shaker technologies are still used at the laboratory and research and development stages because of their cheap costs and versatility. Biotechnology labs use bacteria to amplify the useful DNA material needed for the formation of clones from yeast, animal, insect, plant or human cells. Shaker flasks [Buchs et al., 2000] have proven to be simple and slight modifications such as baffles already increase the mixing effect and thus the yield, whether it be in number of bacteria or copy number of plasmids. Moving from the mL to the litre scale does not require a change to the machinery. This strategy of keeping methods simple and hassle free has now been applied to the culture of animal and human cells.

An interesting and novel approach is the Wave® bioreactor [Haldankar et al.], now property of GE healthcare. This disposable bioreactor uses the tilting of a surface to create a wave going from one side to the other. This is a very gentle and linear movement. Other bioreactors attempt to increase this mixing by almost throwing the culture to the other side of the culture bag. This can be seen in CELLution Biotech's CELL-tainer® which can be classified as 2-dimensional mixing (lateral and vertical mixing). The last two examples are again new developments which approach the problematic from innovative and novel ideas.

Shaking technology has been overlooked and a detailed insight needs to be done to show its performances. The first main question which should be answered is: **Is homogeneous mixing occurring**? And the second: **Is gas transfer at performing levels**?

Materials and methods

Spectrometre Art 200000290 ph-1, mini set with single channel.

pH SensorSpot SP HP5 D7-S SN: 0736-01, PreSens GmbH

Kuhner ISF-4-W, CO_2 5%, Humidity 85%, 37°C, TubeSpin 180 rpm S/N: 17001.51

Kuhner ISF-4-W, CO_2 5%, 37°C, bottles 180 rpm S/N: 17001.6

Tubespin® minibioreactor 50 mL, TPP

Cultiflask 50, minibioreactor 50 mL, Sartorius

CHO DG44 ($dfhr^-$) cells adapted to suspension cultures

proCHO5, CDM cell media, LONZA

pro293, CDM cell media, LONZA

Glutamine, Sigma Aldrich, G5763

Phenol red, Sigma Aldrich, P3532-25G

simHBS (simple Hepes Buffered Saline) 20mM HEPEs, 150mM NaCl, 5 mg/L phenol red

repelcote VS, BDH, Poole GB, batch J4-163, art: 63247 4U

pH meter 691 Mettler Toledo AG, Scherzenbach CH, art. 1.691.0010 S/N OM4/197

Mettler Toledo autoclavable ph electrode, InPro 3200SG/325/Pt100 art. 52001817

pH meter 340 Mettler Toledo AG, Scherzenbach CH, S/N M4366

Mettler Toledo pH electrode, Inlab Expert Pro

calibration buffer 4, Fluka

calibration buffer 7, Fluka

calibration buffer 10, Fluka

rec 111, GE healthcare, S/N REC111000050

Panasonic DMC-LX2 Lumix camera

NOVA Bioprofile 200

Cell culture passaging every 3-4 days by reseeding to $5x10^5$ cells/mL in fresh media

Cell defrosting: resuspention in 20ml Media in TubeSpin minibiorector. Reseeding 24 hours later at $5x10^5$ cells/mL in fresh media

Chapter 1:

Mixing analysis

Introduction

Mixing of liquids can be classified as the involvement of turbulent or chaotic liquid flow [D. Gerson]. And chaotic flows are described using the interaction of the great range of eddies. Gerson goes on in generalizing that the mixing regime can be characterized bay a power spectrum, or a plot of the log of eddy intensities vs log of eddy frequency.

Two types of mechanisms are available to produce an orbital shaking platform. The platform must only move in a translational manner on a fixed plane. No rotation of the platform is allowed and vibrations must be limited to a minimum. To understand the two mechanisms available on the market, a quick look into the basic design is necessary. The first design, which is the most common, is the use of three rotational points to guarantee a planar movement. The three points are connected to the shaking platform with three identically long arms which have a length of half the shaking diameter. As an analogy to railway steam engines (fig. 3) using a connecting arm to ensure that all wheels are turning at the same speed, the connecting arm in shakers is positioned as a triangle.

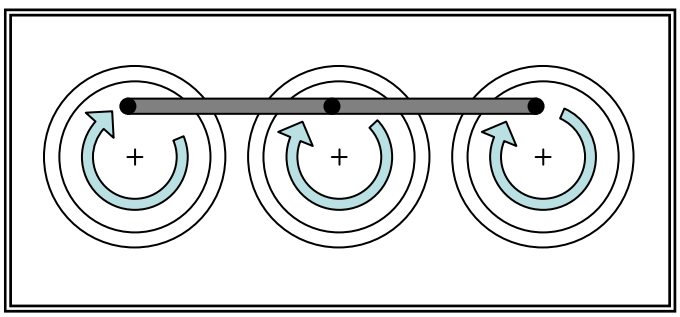

Figure 3: Steam engine wheel connection analogy

As long as the three rotating axis are perfectly parallel to each other, the shaking platform will be moved on a perfect plane perpendicular to the three rotating axis. This is represented by the next figure (fig. 4). The counterweight plays an important role in equalizing the now off centred shaking platform weight. This is only important on the driving axis, as the strain of this off centred weight is only felt by the motor axis. The two other eccentric bearings only act as support and guidance of the shaking platform to the defined movement. This type of shaking mechanism is used by most shaker manufacturers such as Sartorius (previously BBI), Infors and Heidolph.

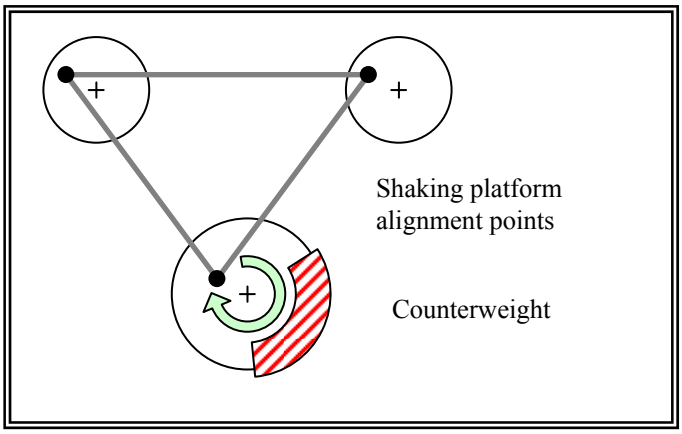

Figure 4: Triple rotating axis shaker mechanism

The second shaking mechanism uses only one eccentric bearing directly connected to the motor. This technique shows that the movement of the platform is purely a translational movement composed of two perpendicular movements. To obtain this movement, two deformable parallelograms are used. The deformation of the parallelograms is possible by using the bending properties of metal blades. Two sides, opposite to one another, of the parallelogram are made up of metal blades (fig. 5A). Two of these parallelograms are mounted together at ninety degrees to each other with the second parallelogram mounted on the moving side of the first parallelogram. This guarantees that the moving side of the top parallelogram will move on a perfect plane and is directly attached to the shaker platform. The eccentric driving force is then attached to the platform.

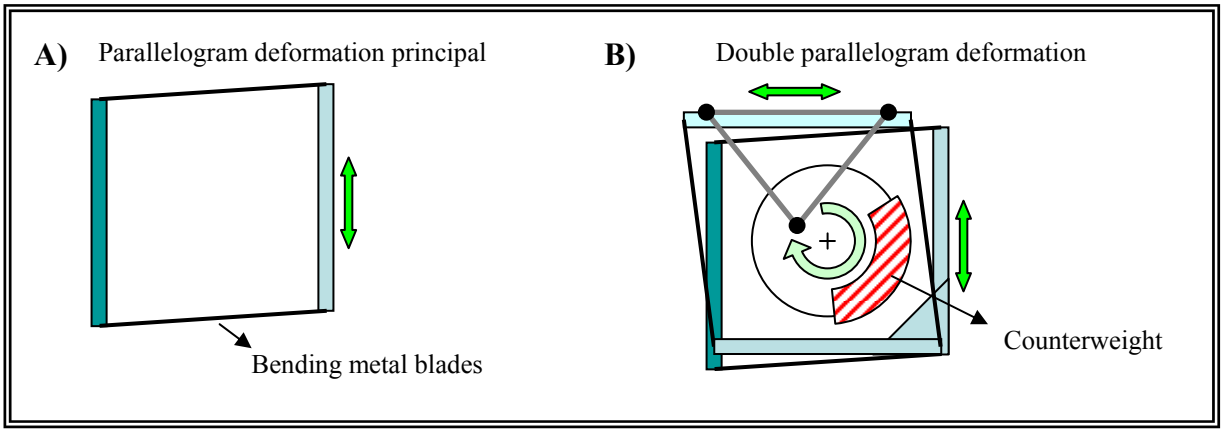

Figure 5: A) Parallelogram deformation principle, B) Complete double parallelogram mechanism

Again the counterweight is attached to the driving axis to compensate the eccentricity of the shaking platform movement. This mechanism (fig 5B) has less rotating parts which is an advantage for the working life span of the shaker as there are less friction points. The double parallelogram is almost indestructible during normal usage as the strain on the parts does not exceed the elastic deformation properties of the material. The resulting movement is a perfectly circular movement of defined diameter, represented by the following top view figure (fig. 6). The three attachment points are also represented in the triple rotation point system (fig. 4) and the double parallelogram system (fig. 5B).

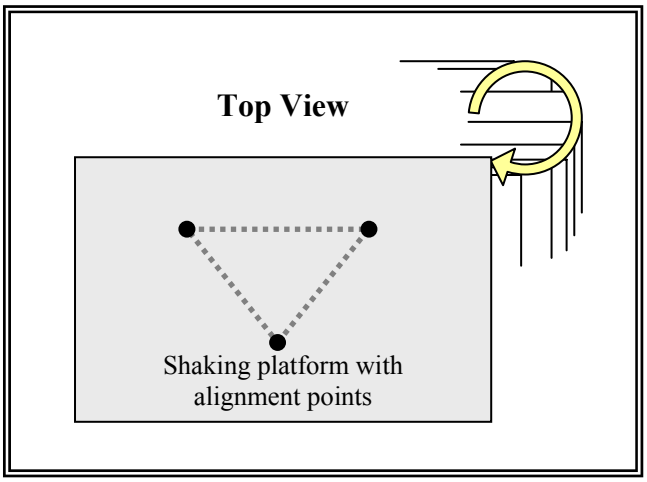

Figure 6: Shaking platform defined movement

In this chapter the experiments are aimed at observing the mixing phenomena using visual methods. The first observations were made using two liquids of different densities and observing the way they mixed. The force of the mixing was also tested on heavier particles, in this case sea sand. By varying the speed of the agitation and the shaking diameter on various cylindrical vessels, observations were made on the shape the liquid was forming.

Materials and methods

Enough sea sand was put in the 28 cm diameter vessel to form a 2-3 mm layer of sand at the bottom of the vessel containing 10 cm of water. The shaking speed was then varied from 40 rpm to 140 rpm by 10 rpm increments. Using a mixing rod, the sand layer was reformed after each shaking sequence (40 to 140 rpm) and an additional 2 L of water were added. The visual observations were made on a subjective scale from 0 to 5.

Different size cylinders (radius = 15, 30, 86 and 144 mm) were placed on the same shaker filled with water at a height to radius ratio of 1. The shaking diameter was changed to 12,5 mm, as apposed to the normal use of 50 mm shaking diameter, and observations were made on the shape of the liquid's surface.

A 600 mL beaker was filled with 50 mL of commercial food grade raspberry syrup to which 200 mL water was slowly poured over the top so as to obtain two visible layers. The speed of the shaking was then increased from 70 rpm by 10 rpm increments and the observations were noted.

Similarly, 200 mL of water and 50 mL food grade oil was put in a 600ml beaker. The observation were done while increasing the shaking speed by 10 rpm increments. This experiment was then repeated with a beaker treated with repelcote®.

Results

For the sea sand experiment there is a tendency (Table 1) to decrease the intensity of the flows near the bottom of the vessel as the level of liquid increases. A double wave forms at 70 and 80 rpm for all, except the 6.5 L column which only shows a double wave at 70 rpm. The NA indicates that the shaker was moving due to the centrifugal force.

Table 1: Bottom flow intensity

		liters				
		6.5	8.5	10.5	12.5	14.5
rpm	40	0	0	0	0	0
	60	0	0	0	0	0
	70	2	1	0	0	0
	80	3	2	2	1	1
	90	4	4	3	3	3
	100	4	5	4	4	4
	110	4	5	5	5	5
	120	4	5	5	5	5
	140	5	5	NA	NA	NA

code	movement
0	none
1	slight
2	moderate
3	high
4	lift sand
5	mix sand

The change in diameter to 12,5mm had visibly no double wave effect on the 15 and 30 mm radius vessels. It is very difficult to see what is happening in these two vessels at high shaking speeds. The flow is regular and the slope of the liquid increases with an increase in shaking speed. The two larger vessels show three different deformations. The first at low speeds is simple deformation of the liquid at what seems to be perfectly regular and smooth i.e. there is no visible difference between on rotation and the next. At 70 rpm for the 144 mm vessel, a slight double wave appears with a pause approximately at the median position of the wave. This is referred to as the double wave type 2 (fig. 7). At 90 rpm, the 86mm vessel showed a type1 (fig. 7) double wave. In comparison to a 50 mm shaking diameter where only the 144 mm vessels shows a type 1 double wave at a shaking speed of 70 to 80 rpm.

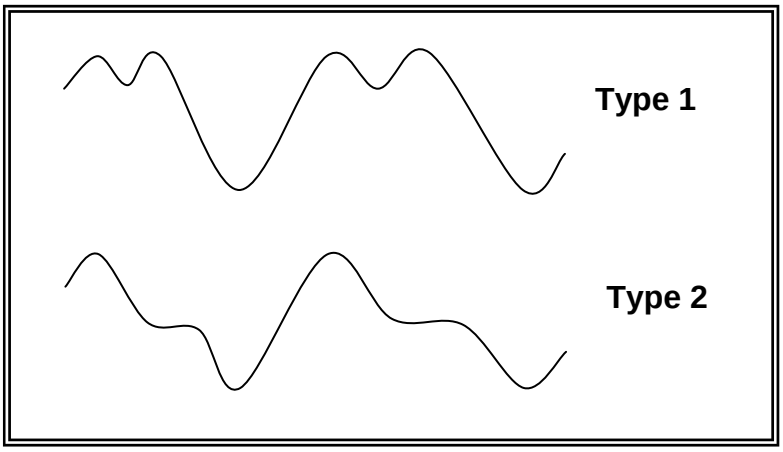

Figure 7: Double wave types

The speeds higher than the double wave speed send the liquid into an inclined vortex as in figure 8. There is a formation of a breaking wave gargle every 6 to 7 turns at 110 rpm for the 144 mm vessel and similarly every 5 to 6 turns at 130 rpm for the smaller 86 mm vessel.

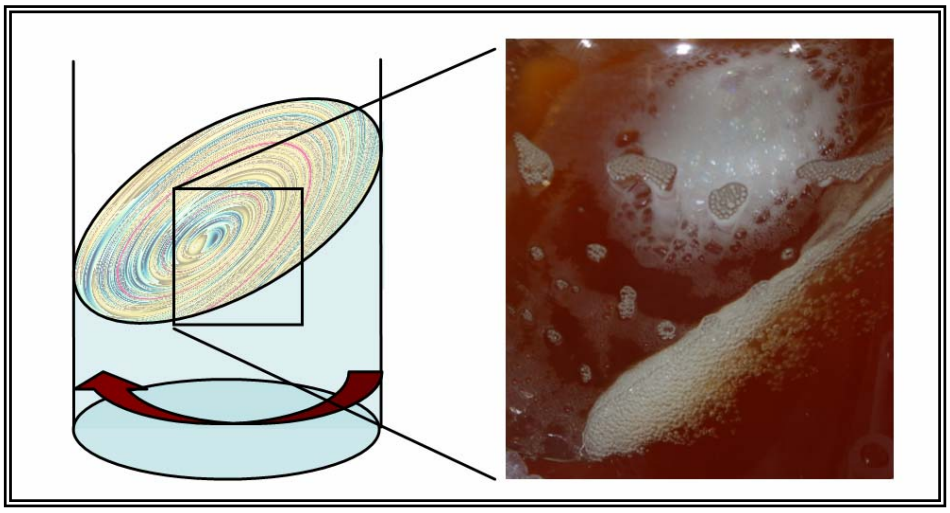

Figure 8: inclined vortex illustration and fronting wave

The syrup and water idea did not reveal much about the mixing effect. It showed an accumulation of the denser syrup near the centre of the vessel and an upward force affecting the syrup near the sides just after the passing of the wave's low level. These observations started at a speed of 100 rpm.

The oil and water showed the effect of the inner surface of the vessel. The untreated beaker could reach 110 rpm before a mixing effect occurred. The treated beaker needed 20 more rpm to achieve the same result.

Discussion

These experiments show that there are three levels of mixing action; the simple liquid deformation, the double wave stage, and the inclined vortex. The most interesting mixing appears to be during a later phase of the inclined vortex. The irregular formation of a breaking wave noise indicates that turbulences are pushing the wave to break every now and again. A breaking wave does implicate high shear forces, but the advantage is in the gassing of the liquid. A hypothesis can be established saying that cultures should be shaken at the speed of the first visible breaking wave. A second idea is that since a vortex is forming, a soft flow of the liquid towards the centre and down as an analogy to a whirlpool.

First image analysis at 50 rpm

Objective

Have a graph that can show the evolution of the liquid level on a fixed vertical axis defined on the vessel's surface. The result should be the same for every other vertical axis on the vessel's surface. This is at 50 rpm which is in the first level mixing, consisting simply of liquid deformation.

Materials and methods

Using the camera fixed to the shaker platform, the lens at the same height as the liquid (17cm) and a ruler stuck vertically to the surface of the 28cm diameter vessel, with the liquid level at the middle mark of the ruler. The camera is set to film in 16:9 format at a pixel definition of 848x480 and a frame rate of 30 fps. The camera angle needs only cover the length of the ruler.

One minute of film is taken and played back on a computer, where frame by frame the value of the water level is measured on the ruler. This is painstakingly slow as there are 1800 pts to enter manually into a computer.

Results

The graph that is produced (fig. 9) shows that the periodic movement starts at around 40 seconds. It took the shaker just under 4 second to accelerate to the given speed, but for the liquid to even out the acceleration impulse, it took the whole forty seconds. The 50 rpm periodicity was confirmed by same value displacement levels are separated by 1.2 seconds corresponding to 36 data points. The next notable fact is that the level descends to -1.5 cm but only rises to 1 cm.

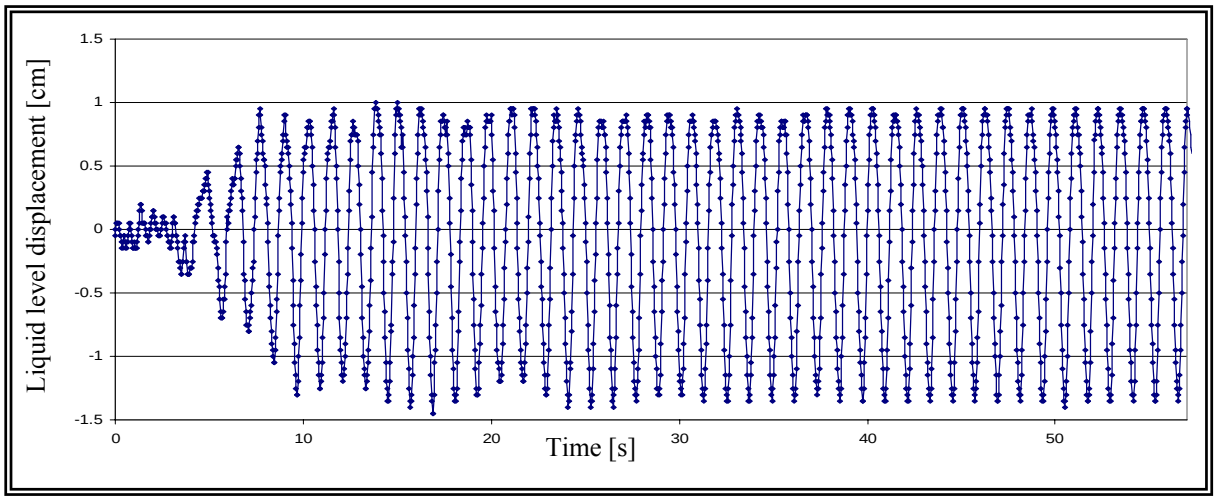

Figure 9: Liquid level displacement over time on a fixed vertical axis.

A close-up view (fig. 10) of a portion of the graph after the 40second equilibration phase, shows more detailed information. There are 16 data pts below the zero and 20 points above. The down slope is -0.15 and the up slope is steeper with a value of 0.21. The integration of the negative and positive surfaces shows which area has the most potential energy. The value for the positive displacement integration from 40 to 40.6 s is 0.465 and the negative integration gives an absolute value of 0.437. The difference of 0.028 is suspected to be part of the energy transferred to the vessel by the shaker just to maintain the shaking speed.

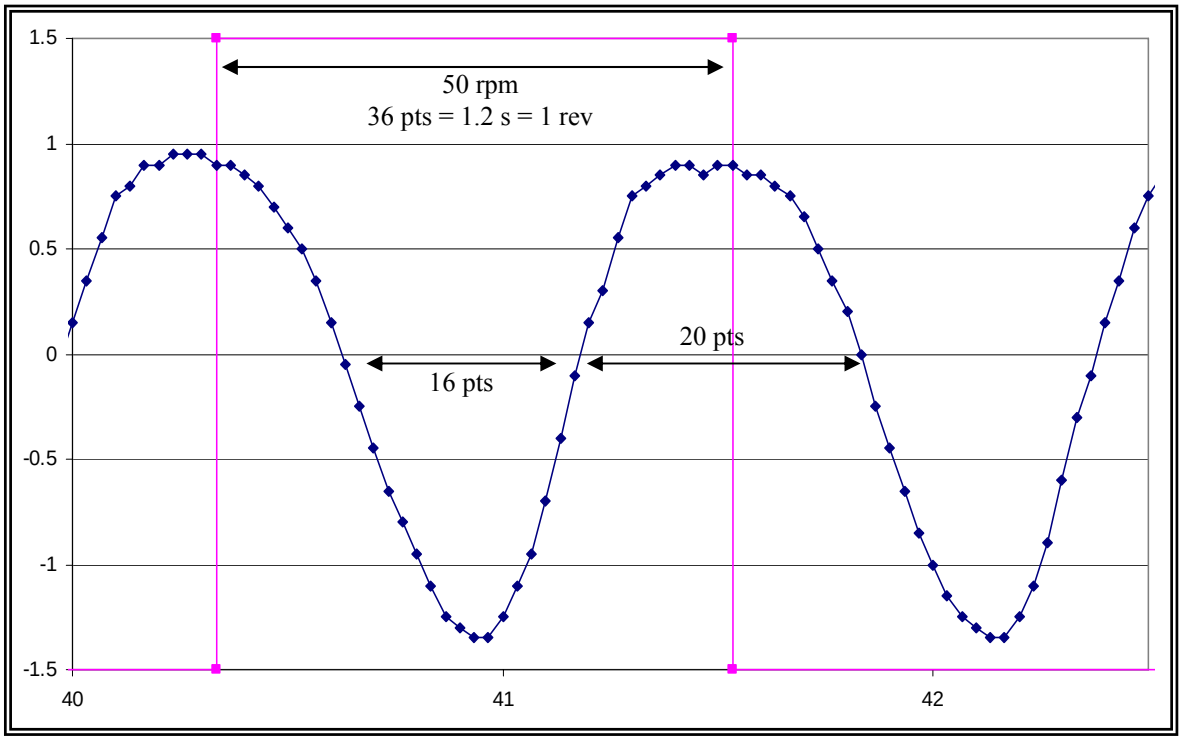

Figure 10: Close-up view between 40 s and 42.5 s of liquid level displacement over time

Discussion

This whole analysis is only done on the perimeter of the vessel. The calculation of the potential energy is of no value in this scenario. The difference in slopes is mostly due to the inner surface of the vessel. It is not smooth and thus the rising liquid level is prevented from rising normally due to this friction and the falling slope is held back as the water cannot detach itself from the wall. This can be seen as an analogy to a drop of water sliding down a surface; its front end preventing it from advancing normally and its back end producing a tail. The hypothesis previously noted that this speed isn't sufficient to produce a double wave seems to be proved wrong. There is already a slight holdback of the liquid and a plateau of around 0.2 s is already visible on the high level.

Development of an image analysis logic using ImageJ

The mixing evaluation has to go through the stage of observing the physical happenings. An evident observation is the rise of the liquid level on the side of the shaker vessel. Once this is measured it can be compared to computer simulations or approximations using simplified mathematics and physics. The observation of the water level can be made with a camera. The speed of the camera has to be quite high as the revolutions per minute used are all over 1 turn per second i.e. the frame rate has to be quite high. The resolution of the camera also needs to be elevated to be able to distinguish the water level on the side of the vessel. High speed cameras with elevated pixel definition are heavy and expensive. The standard video camera rarely has a definition higher the 800x600 which is the definition of a preHD television. The frame rate is at 24 or 25 frames per seconds which is the refresh rate needed for the human eye not to notice the fixed frame and distinguish fluid natural movement. The camera needed to be light to attach it to the moving platform. The referential therefore being the vessel surface. This referential is moving in a translational manner. The movement of the vessel due to the displacement of the vessel and contents on an eccentric plane can be accommodated by the image analysis software using defined referential points. The camera having a very small lens, gives a deformation of the real image especially near the corners of the visual site. This can be accommodated using image analysis and correction but at this stage the precision is not needed within these parts of the rendered picture.

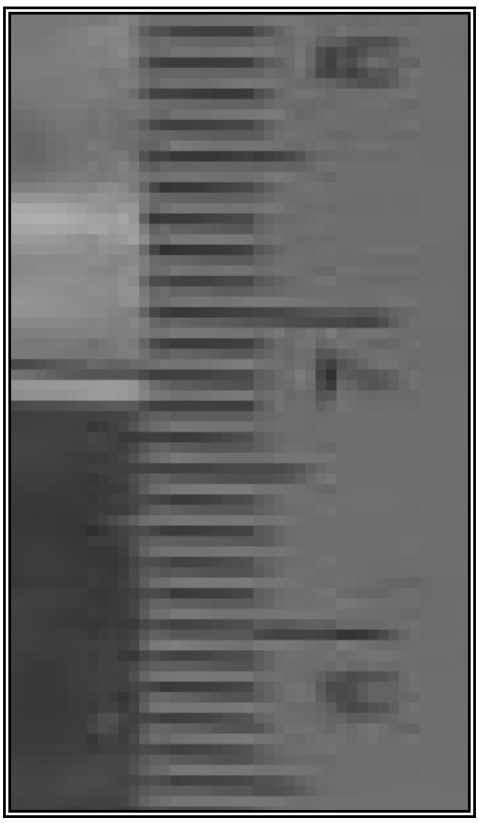

Figure 11: Pixelized ruler image

To take the film the camera is positioned to film the whole vessel with the minimal amount of exterior views. The edge of the camera is aligned with the edge of the vessel. The camera has a resolution of 480 pixels in width and the vessel is 30cm wide thus one pixel is about 0,625mm. A millimetre marking on a ruler is smaller than half a mm therefore the resolution of this marking will already be blurred and not easy to distinguish. Figure 11 is from the first tries using the camera with a ruler stuck onto the vessel. The blurry affect mentioned is clearly visible.

The first part of the image analysis is the separation of the movie file into separate images so as to work on each image independently. The camera takes 30 fps in a wide view format 848x480. This is not a standard format size. The compression format is a .mov file which is a multilayer encoding system. Images and sound are separated which improves the image quality when they are decompressed. This file format was developed by Apple Incorporate for the Quicktime application. Although many programs can read this format, the only way to export the images is with the Apple proprietary software Quicktime Pro. This was necessary, as the memory (stack) needed for ImageJ to open a whole movie file (at least 1 minute of film) is out of range of most personal computers. With 512MB of virtual memory, I was only able to open 15 second of film. The solution to export the film through Quicktime Pro is possible and necessary as all the other programs such as Final Cut Studio, Motion, iMovie readjust the image to a 720 pixel width or even convert the image rate to 24 or 15 frames per

second. The conversion to 720 pixels reduces the pixel definition, which is already very low, by a whole 15%. The Quicktime Pro has a useful export function into numbered separate images using a bitmap compression which guarantees no loss of information due to it memorising of each pixel. In comparison, a jpeg compression would loose information as it is an approximation using the Fournier equation solutions. The exporting of the images is done in an 8 bit grey scale as colour is not necessary in seeing a water level. Converting to a grey scale does not reduce the quality of the image as long as the colour scale was also in an 8 bit format.

The images must still be rotated by ninety degrees to the left by selecting all the images in the folder and using an option in the right click mouse menu allowing this.

The global analysis approach is to run 3 consecutive macros, after converting the movie to usable images, as described in the linear process analysis diagram (fig. 12).

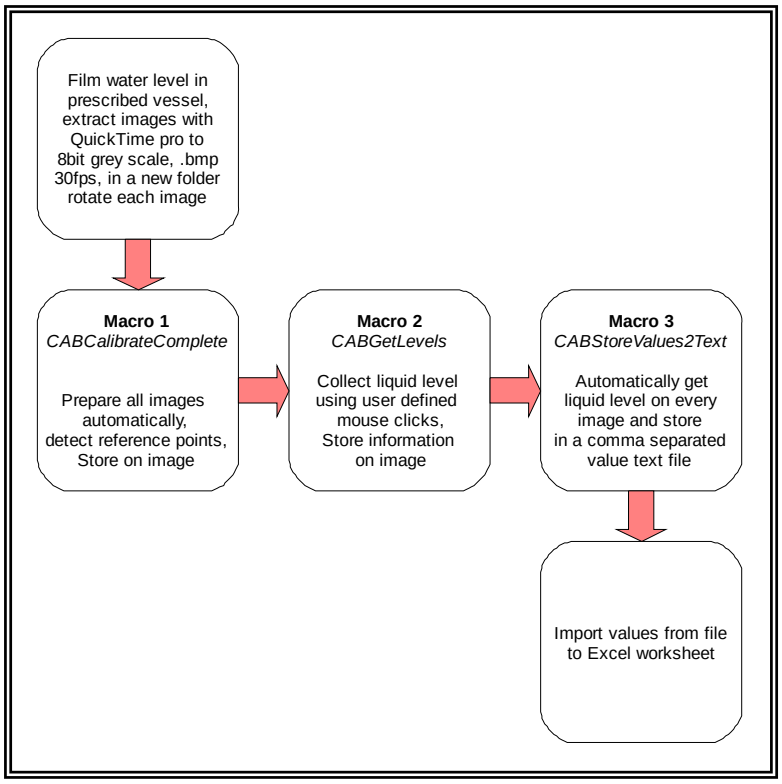

Figure 12: Linear process analysis diagram

Once the film has been taken, and the images separated and rotated, the image analysis can begin. The program used is ImageJ, a freeware under the GNU General Public License. It has built in functionalities that are easy to use under the form of macros. The whole program is built using Java and can also be implemented using java code as the programming language. As Java is a more complex programming language, it is better to use the built-in macro language as a first step to a robust specific image analysis of a liquid level on a vessel surface.

The shaking vessel needs reference points on its surface to be able to calculate the height of the liquid. Unfortunately, it cannot be supposed that the vessel will remain in the exact same position on the image. Both the vessel and the camera move slightly due to the centrifugal forces. A best effort is made to secure the vessel to the surface of the shaker platform and the camera, too, is securely fastened, but this is not enough. The reference points are therefore a necessity and the height of the liquid will be calculated using the position of these reference points. When looking from the side of the vessel, only 90° of the vessel can be efficiently seen as is shown in the next figure (fig.13). The camera visual angle must take the whole vessel.

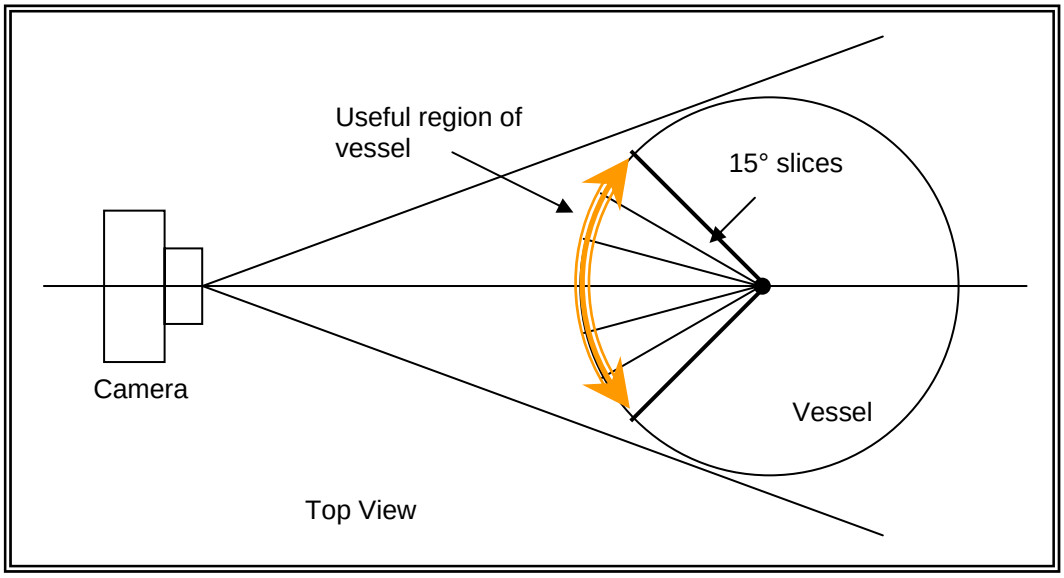

Figure 13: Camera viewing angle schematics

The regions out of the 90° angle are used for the referencing points. The choice of the referencing method was based on the functionalities of the ImageJ built-in macros. As the pixel definition is slightly larger than half a millimetre on the vessel, a crosshair would have to be at least 1 mm thick. Detecting a crosshair is not a simple matter. As it will have to overlap a few pixels, the exact center of the crosshair would be an average. Also, as it is distorted by the curve of the vessel, this will bring more difficulties as it moves. Programming the detection of a crosshair is in the timeframe of this project unnecessary. The solution is using a filled black circle of 5mm in diameter. The built-in macro of particle detection allows the program to automatically find these circles. The detection is not limited to circles. It can find any ellipse even if it is not horizontal or vertical. The part of the ellipse that does not change from the real to the distorted image is the center, and the center is a parameter that is automatically exctracted into the results window.

In the picture (fig. 14) here below, the deformed ellipses as they appear on the image are all from an original 6mm filled black circle.

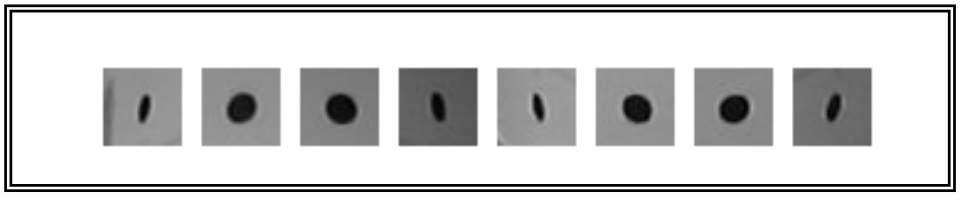

Figure 14: Deformed circles due to curvature of the vessel

The positions of these black dots are defined above the horizontal middle of the vessel which is, as a choice, the liquid fill level. This middle is also as close as possible to the middle of the camera. It is best to represent this with the image of the actual alignment template (fig. 15) used and its image as seen by the camera. The reference points are clearly visible and stand out against the white background.

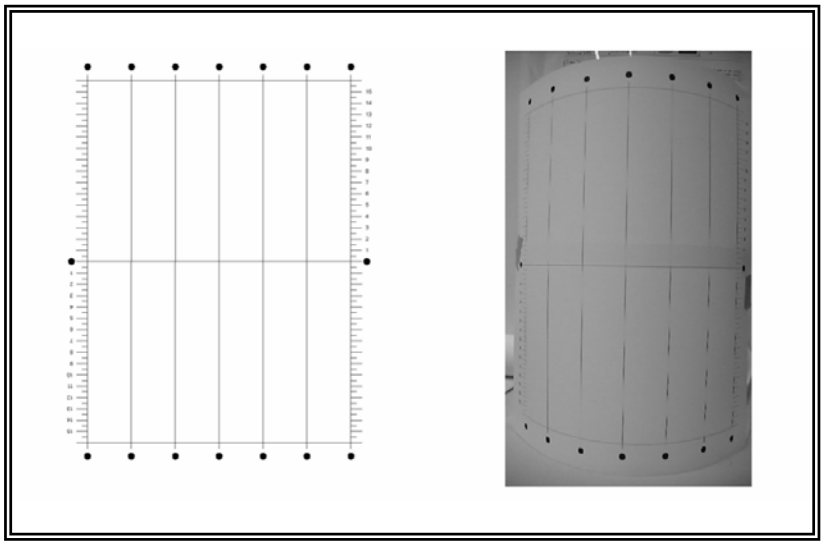

Figure 15: Alignment template model and image from camera

Although there is a great visual change in position of the referential dots, the linear division between to vertically aligned points does not change. This means that by taking the distance between two vertically aligned points and dividing it by the real number of millimetres will result in a pixel/mm conversion. The correlation between the pixels and the millimetres is linear. This is proved by taking a photo of equally spaced square dots (fig. 16 left); in this case, 25 vertical and 43 horizontal dots. This corresponds closely to the 480x848 ratio as the 25 versus 43 dots makes a distance of 12cm by 21cm which is a 1:40 scale of the true pixels. By taking a picture of this calibration framework in high definition, the resulting image (fig. 16 right) shows the deviation of the optical system of this camera. With the exception of the corners and the exterior boundary, the image is true to the template model.

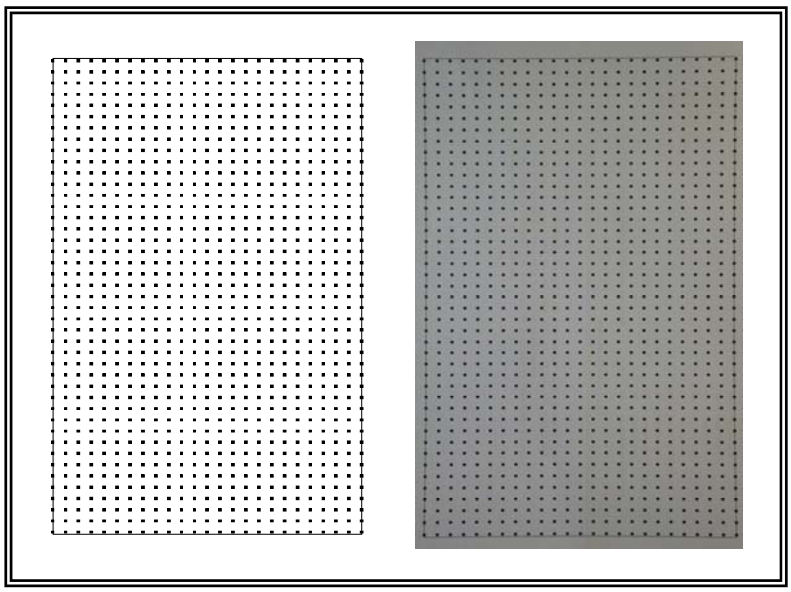

Figure 16: Camera linearity restitution page and image

To store all the information from the images, the decision was taken to include it in every image (fig. 17) through pixel encoding. Pixel encoding is taking numerical information and placing it in an image as a pixel. Thus every digit of a number is stored as a colour. The pixels are in an 8 bit format, allowing 256 colours and potentially any value from 0 to 255. The size of the image is 900 by 848 pixels and thus exceeds 256, thereby forcing the use of one pixel for one digit of a number. Visually the human eye cannot distinguish between two pixels of which the grey intensity difference is under 10. For example a pixel of value 2 is visually the same as a pixel with a value 12. Look up tables (LUT) can make this visible by associating a pixel value to a colour visually recognisable from a second pixel of value one higher than the first pixel. The use of LUTs would be a method to distinguish the water level automatically but this type of image analysis is highly advanced and requires subsequently hours if not days or weeks of programming and testing to evaluate the algorithms used. A modification in the position of the light source can render an algorithm absolutely useless. Thus, I did not use LUTs in the development of the algorithms and restrained myself to using the image analysis only to simplify the extraction of water level distance from the reference points.

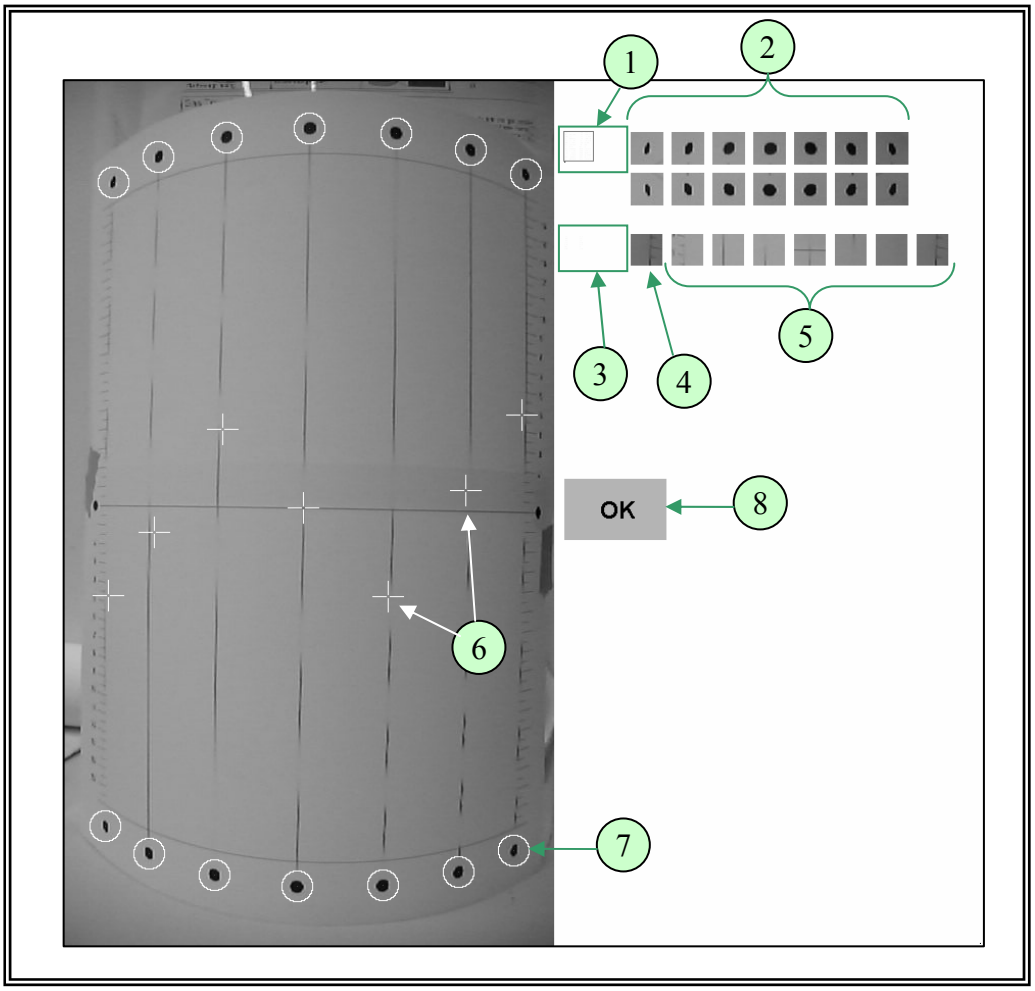

Figure 17: Analysed image canvas after 2nd macro

Legend: 1)Pixel encoded position of reference points, 2)Images of reference points used to erase circles, 3) Pixel encoded crosshair position, 4) Current cursor location image, 5) Level cursors' images before drawing crosshair, 6) Crosshairs indicating liquid level, 7) Visual confirmation of reference points' center, 8) Confirmation of completely analysed image.

The logic behind the approach to finding the reference points can be seen in the diagram (fig. 18) here below. This is the flow diagram of the first macro titled CABCalibrateComplete of which the code presented in appendix XXX. With the exception of selecting the first image of the analysis and clicking on each reference point in that image, the whole process is automatically done until the end of the images in the folder.

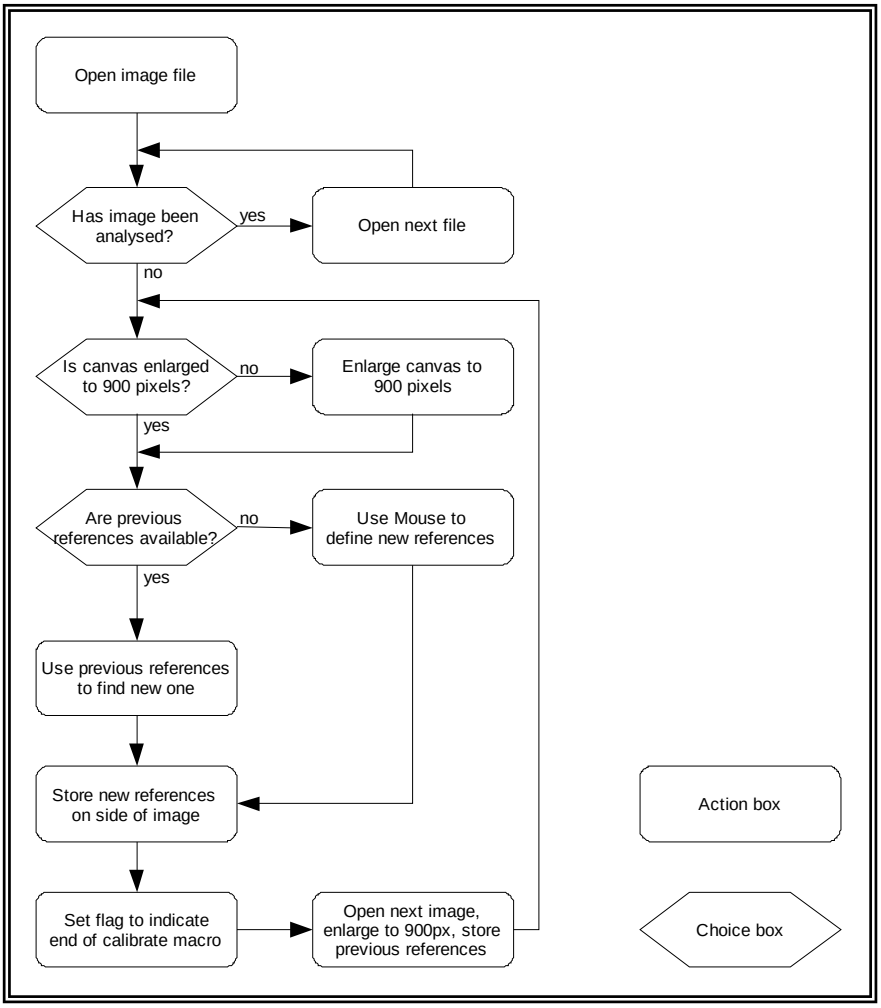

Figure 18: Logic behind macro 1 titled CABCalibrateComplete.txt

The next macro, CABGetLevels (fig. 19), has the most time consuming process for the user. There are 7 liquid level points per image to validate with the cursor. The program automatically aligns the cursor with the vertical reference points thereby facilitating the defining of the point as there is only a vertical component to enter with a click of the mouse. Another aspect of this macro is the back function which when right clicking on the mouse, the user will be able to correct the previous crosshairs. Once all crosshairs are set, the OK sign (see fig. 17 legend 8) appears and users have to click on this sign as a confirmation that the crosshairs are correct.

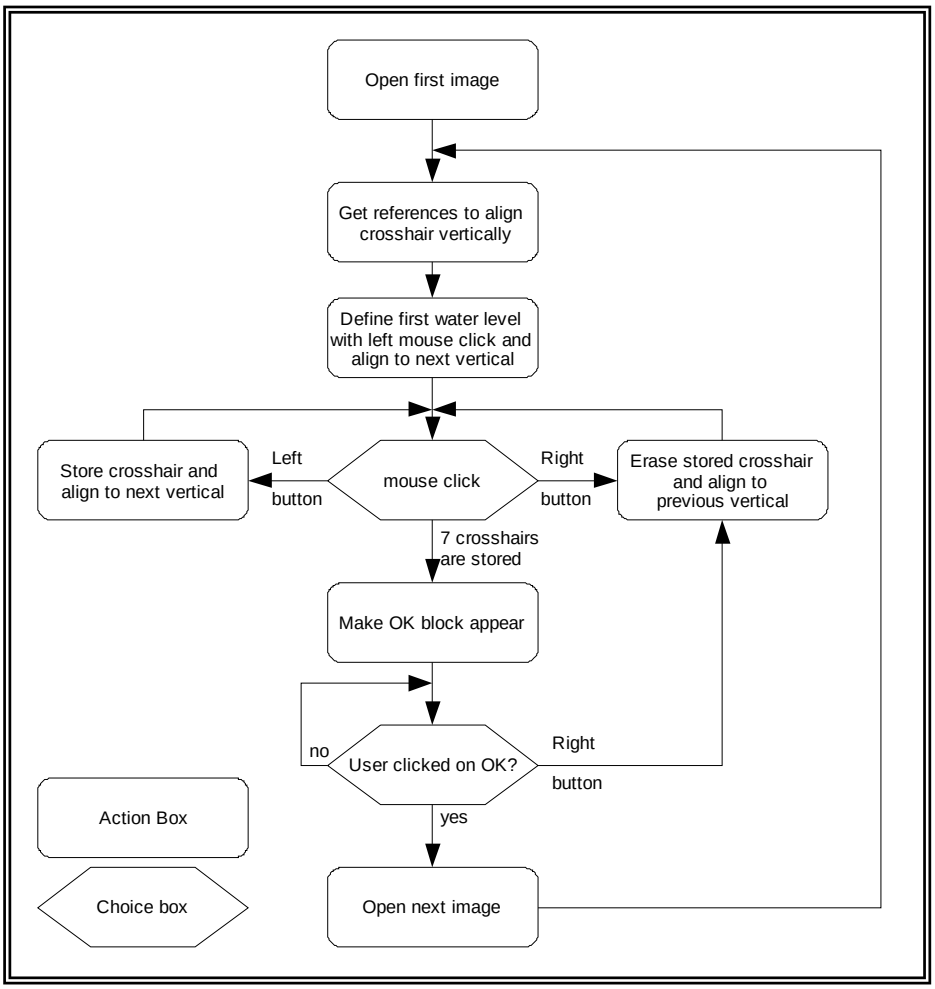

Figure 19: Logic behind macro 2 titled CABGetLevels.txt

Finally, the third macro (fig. 20) is the recording of the values into a same text file. All the information necessary to get the water level in millimetres from the image is encoded on each image using the pixel encoding technique. The conversion from pixels to mm is the quotient of 342mm – the real distance between 2 reference dots – and the distance in pixels of the same two reference dots. The calculated level is a positive (above) or negative (below) value with the zero being the middle point between the two reference points.

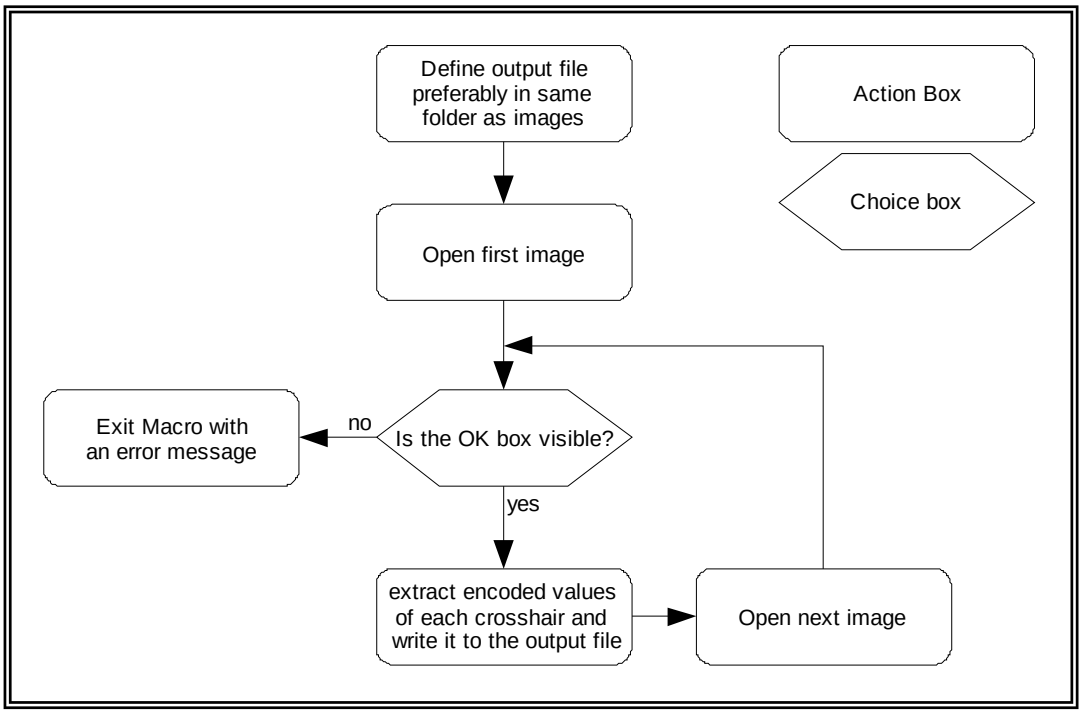

Figure 20: Logic behind macro 3 titled CABStoreValues2Text.txt

Image analysis at 70 RPM

From the image analysis program developed, the need to put it in practice at key RPMs produced some interesting results. The 70 RPM double wave in the 144 mm radius vessel showed the following results (fig 21). The observed double wave is present in the graph but the values at -45 or +45 degrees are not very reliable. The precision of the mouse clicks is still difficult but the speed gained is enormous. A new vessel was used as the old vessel was largely scratched on the inside. Unfortunately, there was no visible difference to the old vessel as is shown by the surface effect experiment described at the beginning of this chapter.

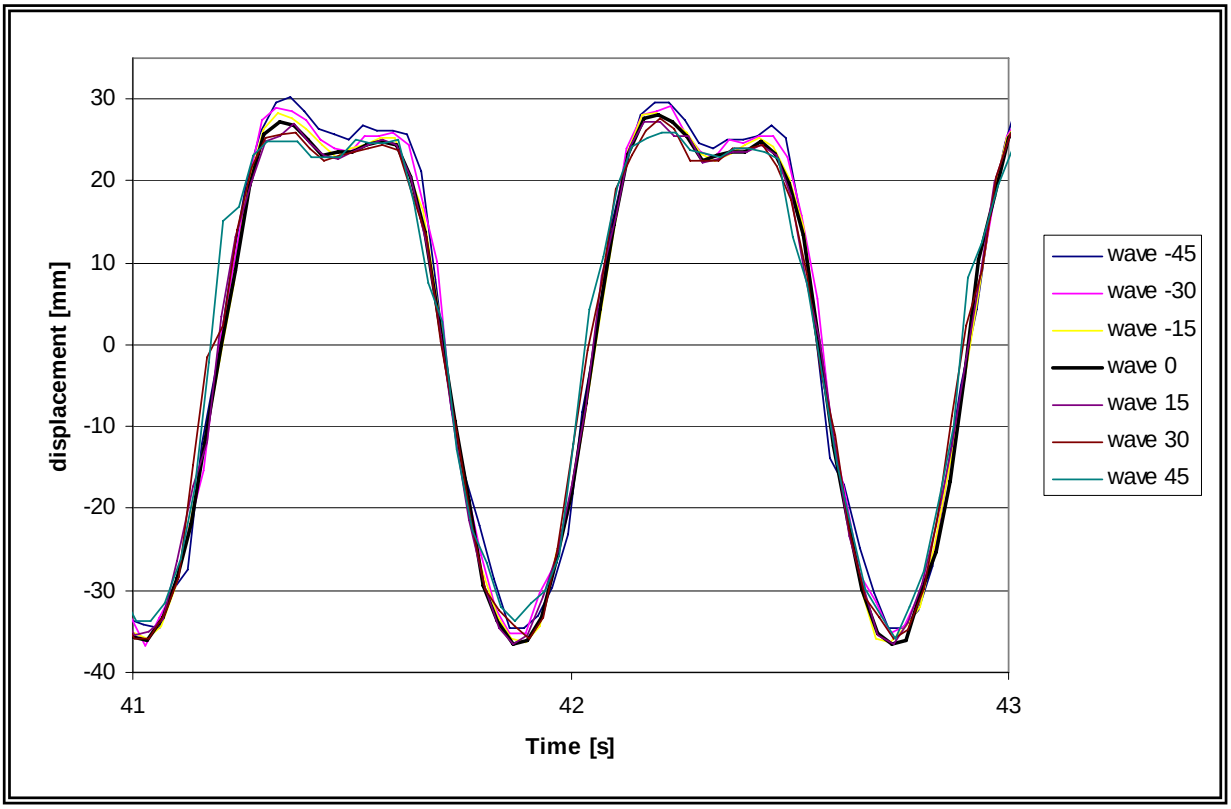

Figure 21: Double Wave closeup at 70 RPM

The agitation speed of 70 RPM allows 25.7 frames per revolution and there was already a blurring effect due to this speed. The meniscus position was largely estimated causing the large differences in the values as can be seen by the graphs that aren't perfectly aligned. This is only partially an issue as the 5 mm variation as can be seen on the first peak is under 8% of the total amplitude. The low level of the liquid is still lower than the high level as was observed in the 50 RPM analysis.

Image analysis at 110 RPM

This higher agitation speed drastically decreases the number of frames for one revolution of the vessel. As the number of frames per turn is now at 16.4, the "wave -15" and "wave 15" values together with the middle 0 value increase the total number of usable values per turn to 49. The graph (fig. 22) shows all the "wave" curves and the error is still around 8%.

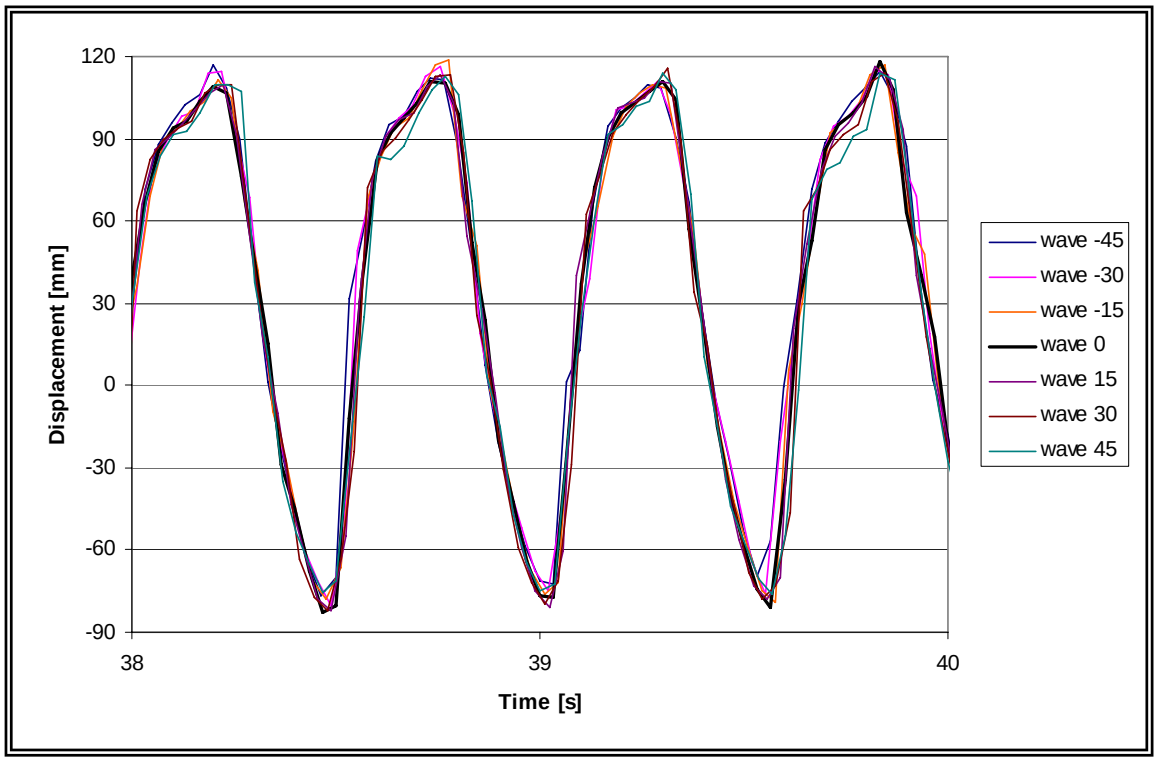

Figure 22: wave (inclined vortex) on edge of vessel at 110 RPM

The interesting phenomenon to take note of is the fact that the liquid rises more than which it falls. In the 50 and 70 RPM observations, these differences are inversed. This mixing structure is the inclined vortex structure. The reason that the graphs do not overlap perfectly again lies with the fact that the water level is moving very fast and it is also much thinner and difficult to see near the top. The bottom level also poses a problem as there is internal reflections and it is not easy to distinguish the exact level. There is also a wave forming on th fronting end of the wave, thus blurring completely this part of the image. A lot of visual estimation of the water level was applied.

The image analysis is a valid method to quickly and easily get basic information, but it should in future be applied with real high definition cameras or other more précis techniques such as laser distance meters, sonar, or low frequency proximity detectors, all of which are non-invasive.

Mathematical approximation of the double wave

The separation of the double wave into a series of single wave equations allows one to hypothesize on the formation of the global wave. The formation of a periodic double peak and single valley can be achieved by the addition of a positive and a negative cosine with the positive cosine having double the frequency of the negative cosine. The smaller valley can be reduced in prominence by increasing the amplitude of the negative cosine. Adjusting the height is merely a constant in front of either equation. To modify the height of the second peak, a sine graph (of same period as the complete double wave) can be added.

$$A_1 - B_1\cos(C_1 \cdot t) \quad \text{negative cosine}$$
$$A_2 + B_2\cos(C_2 \cdot t) \quad \text{positive cosine}$$
$$A_3 - B_3\sin(C_3 \cdot t) \quad \text{negative sine}$$

These equations can be summed to form a simplified version

$$A - B_1\cos(2C \cdot t) + B_2\cos(C \cdot t) - B_3\sin(2C \cdot t)$$

with $A = \text{water level at rest}$

$C = \text{periodicity}$

$B_1 < B_2$

$B_3 < \min\{B_1, B_2\}$

Cosine is a delayed sine thereby essentially it can be said that the double wave is a sum of sinusoidal waves. C is the period and is directly related to the RPM. The coefficients labelled B_1, B_2, and B3 can only be described on a case to case basis. They mark the depths and heights of the valleys and peaks. The negative sine will reduce the height of the second peak of the double wave which is what is observed. Thus a type 1 (fig. 23) or type 2 (fig. 24) can be theoretically formed.

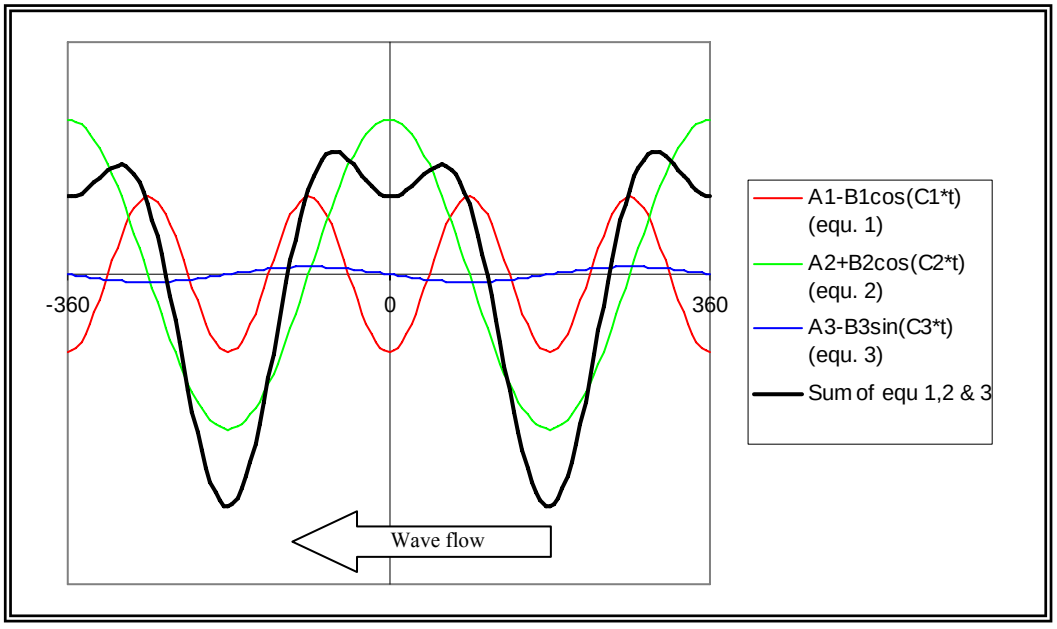

Figure 23: Mathematical reproduction of a type1 double wave with sinusoidal graphs

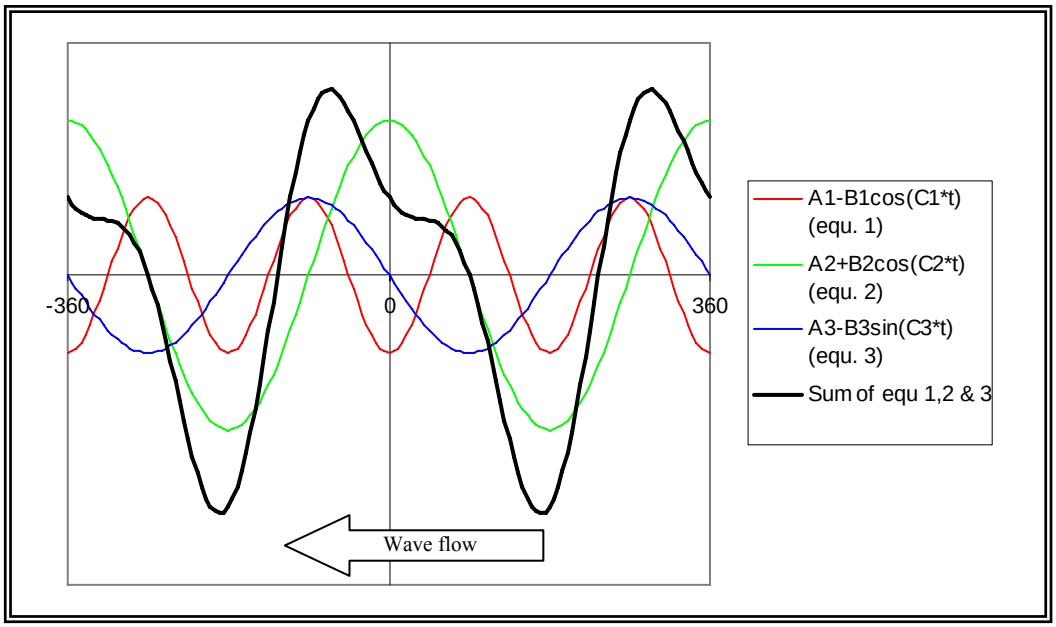

Figure 24: Mathematical reproduction of a type2 double wave with sinusoidal graphs

The two cosines are mathematically the main effect of the double wave due to the doubled period of one of the cosines. Having explained that C is the RPM, the 2C is hypothesized to be a harmonic of the RPM. Thus a slight modification in the mixing either by acceleration, deceleration or friction will bring the harmonic of the first wave. The harmonic and the original wave are maintained due to the RPM. It is not unimaginable that a third harmonic is present but its influence is not noticeable with the methods used to observe the system and it's amplitude is probably too small to actually be visible. Turbulences could also interfere with a higher harmonic's low amplitude and prevent it from forming.

Chapter 2:

Non-invasive optical sensors

Introduction to optical sensors

The oxygen optode sensors

The innovation in oxygen sensors came from the development of non invasive optical oxygen sensitive patches. The previous Clark-type electrodes are seeing their limits in that they consume oxygen and the shape of the electrode also modifies the turbulences in the solution (Tolosa 2002) compared to the electrode not being present. The new sensitive patches are attached to the inner wall of the shaker flask or any surface which has sufficient optical properties for a light signal to reach the sensitive foil and receive the return signal. Shaker flasks are arguably the most widely used vessels for cell cultures in the lab scale but knowing exactly what is happening inside the shaker flasks is mainly overlooked.

Optical oxygen sensors use the principle of dynamic luminescence quenching by molecular oxygen. This has the advantage of not consuming the oxygen as with Clark-type electrodes. The more oxygen molecules are present near the oxygen sensor, the less the luminophore will emit. The following diagram (fig. 25) explains this principle light emission after excitation of a luminophore.

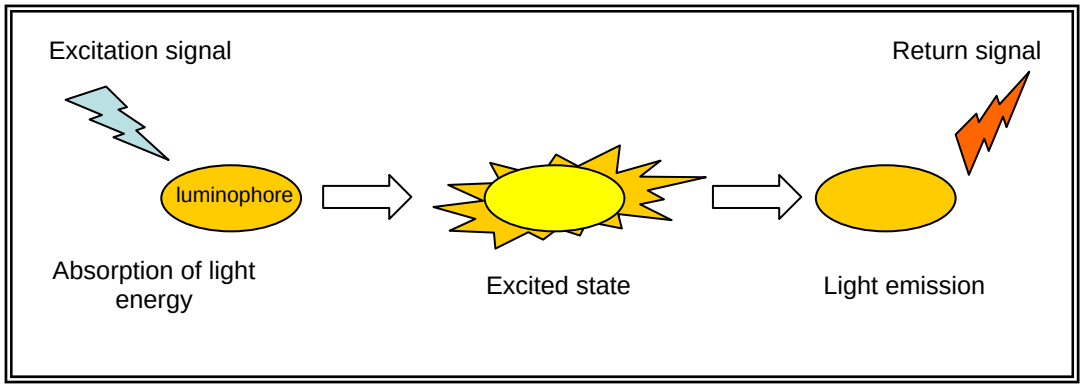

Figure 25: Principle of dynamic quenching of luminescence by molecular oxygen

The light emitted by the luminophore when it returns to its ground state from its excited state is of a different time phase and intensity to the excitation signal. The phase difference is due to the time delay necessary for the luminophore to return to its ground state is used as the basis to determining the oxygen concentration. When an oxygen molecule is in proximity of the excited state of the luminophore, it will collide with it and absorb the energy of the luminophore thereby returning the luminophore to its ground state without emission of light as can be seen in the next figure (fig. 26).

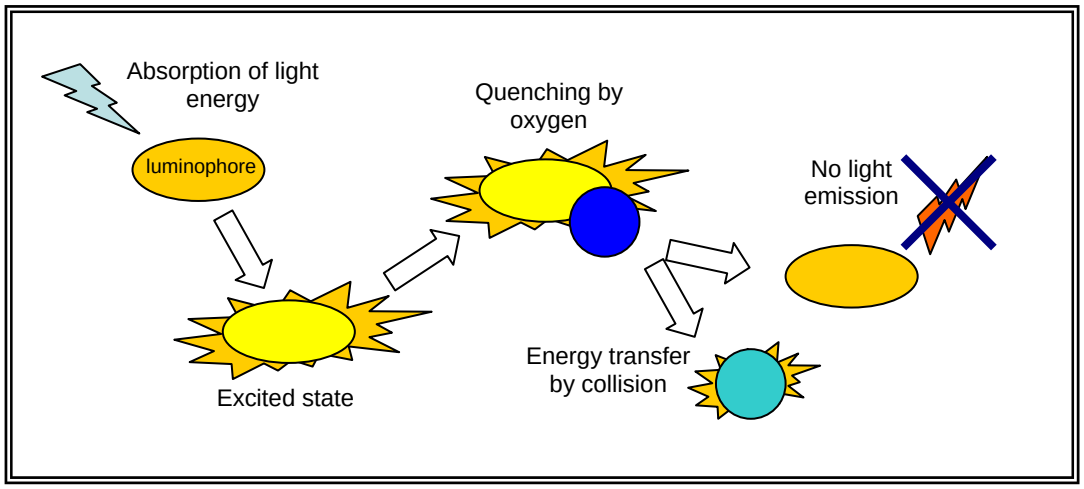

Figure 26: Deactivation of the luminescent indicator molecule by molecular oxygen

The luminescence decay time and the intensity are the two parameters related to the quenching effect which is a function of the Oxygen concentration. The Stern-Volmer equation here below (fig 27) relates these two parameters to the oxygen concentration using the Stern-Volmer constant K_{SV}.

$$\frac{I_0}{I} = \frac{\tau_0}{\tau} = 1 + K_{SV}[O_2]$$
$$I = f([O_2])$$
$$\tau = f([O_2])$$

Figure 27: Stern-Volmer equation

Legend: I: Luminescence intensity in presence of oxygen
I0: Luminescence intensity in absence of oxygen
τ: Luminescence decay time in presence of oxygen
τ0: Luminescence decay time in absence of oxygen

A short explanation on using the luminescence decay time to calculate a phase delay is shown in the following figure (fig 28) available in the operating manual. The input signal is a sinusoidal input and the luminescence decay time causes the sinus response graph to change its phase. The decay time is slowest for an oxygen deprived system as can be seen in the schematic of a single exponential decay and thus moves the graph the most.

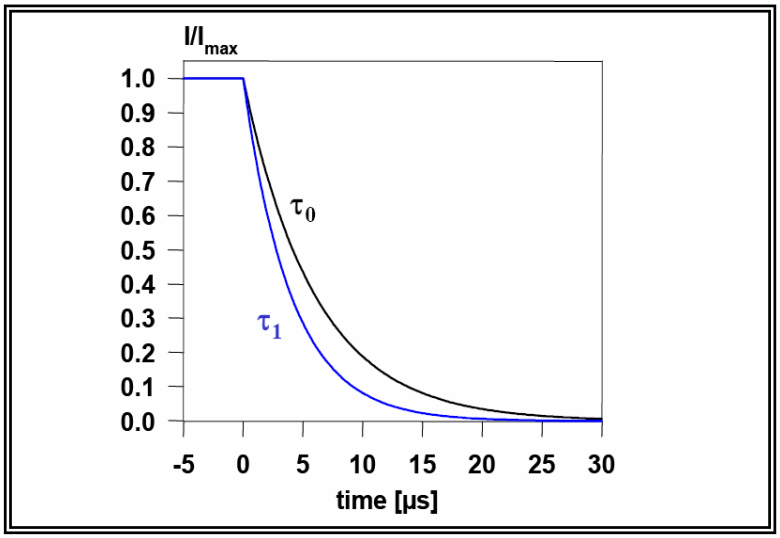

Figure 28: Schematic of a single exponential decay (t_0>t_1)

Depending on the oxygen concentration, the decay time will be sped up as there is less potentially emitting luminophores. This can be seen in the graph (fig 29) showing the reference sinus signal as well as the two measured signals thereby being able to extract the phase (Φ).

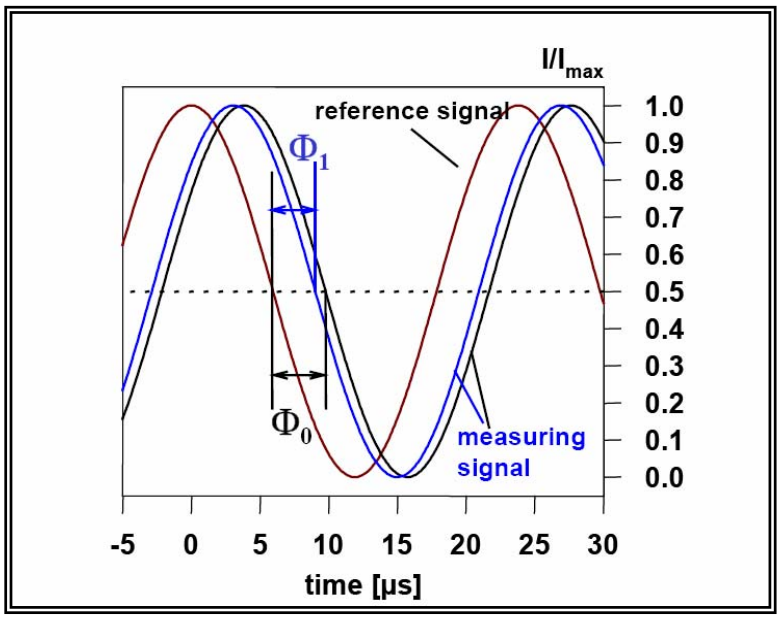

Figure 29: Sinusoidal reference signal and its decay induced phase difference

The relation between **τ** and the phase angle **Φ** used by PreSens sensors in the following equation (fig. 30).

$$\tau = \frac{\tan\Phi}{2\pi \cdot f_{mod}} \quad \Leftrightarrow \quad \tan\Phi = 2\pi \cdot f_{mod} \cdot \tau$$

Figure 30: Equation relating the decay time and the phase angle

Legend: τ: luminescence decay time
Φ: phase angle
fmod: modulation frequency

The phase is a more stable reading method, compared to the intensity, as it is not affected by movement of the optical fiber which may cause signal loss or altered intensity through changes in the geometry of the sensor. Fluctuations of the intensity of the light source and the sensitivity of the detector are therefore not an influence on the reading [PreSens Oxy 4 Manual appendix pg. 55].

The pH optode sensors

The basic functioning of the pH optode is similar to the oxygen optode. The difference being that the luminophore is returned to its ground state by collision with the hydronium ions (fig. 31) instead, thereby similarly altering the phase of the returning signal.

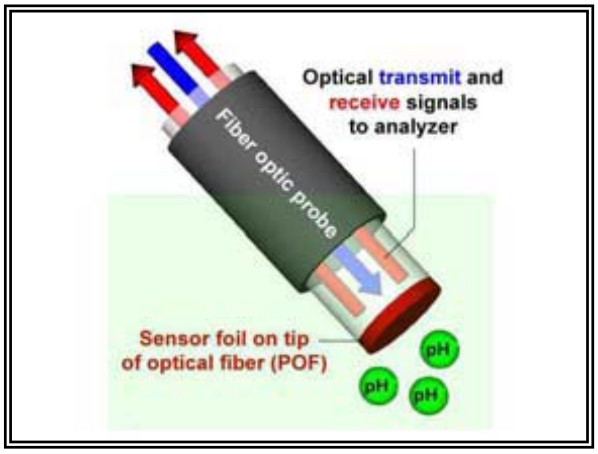

Figure 31: pH optode dip probe

The other innovation in the pH Optode is the use of a dual lifetime referenced (DLR) Optical sensor [Klimant et al., 2001]. Adverse effects [PreSens pH-1 Manual appendix pg. 46] for the quantification of intensity signals led to the development of a novel ratiomettric method where two luminophores with different decay times and similar excitation spectra are used. An pH insensitive µs-lifetime luminophore is combined with an pH-sensitive ns-lifetime fluorophore [PreSens pH-1 Manual appendix pg. 47]. The figure below (fig 32) shows the

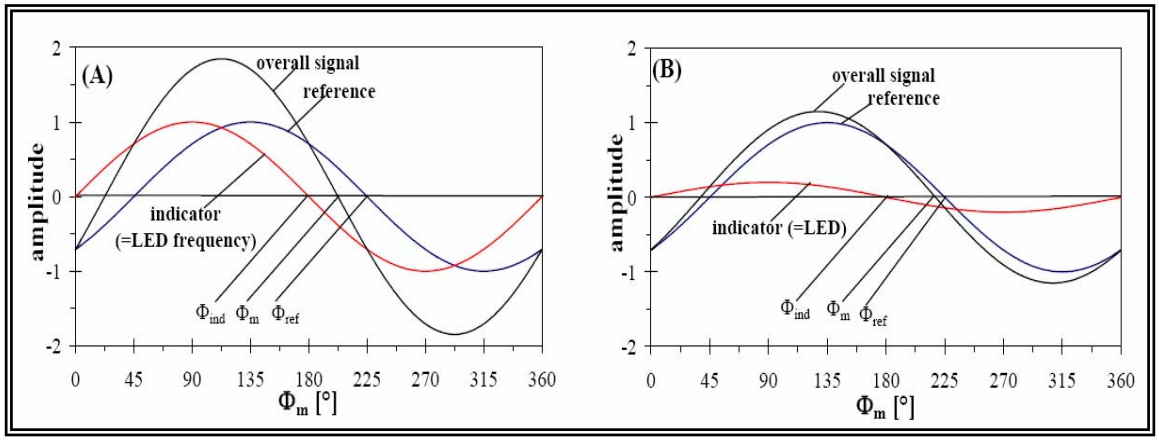

Figure 32: Phase shift of the overall luminescence due to the dual lifetime reference (DLR) system

nanosecond response of the pH sensitive luminophore being of identical phase as the input signal. The ratio is then calculated using the pH insensitive reference

pH Optode reaction time evaluation

Introduction and Objective

The original idea was to use the pH optodes to evaluate mixing time in a 1000 L shaken bioreactor. A protocol needed to be established to have robust results. Unfortunately, the solution of using a simple HEPES buffered saline solution proved to be too expensive for the application in the 1000 L bioreactor. The reaction time of the electrode was tested in water and isotonic saline solutions but there was a constant drift of pH whether it be with the optodes or with a traditional pH electrode. The need was to have a defined step in pH that could be repeated a couple of times. The pH optodes also have a characteristic of having a linear calibration between 6.5 and 7.5. Out of these ranges, a 5 point calibration and must be done, in combination with solving the boltzman equation, to extent the range from 4 to 9. It was only logical to use a HEPES based buffer as it is present in many commercial animal cell culture media. The evaluation of the reaction time of the optodes was therefore done in 20 mM simHBS using defined quantities of base and acid to repeat the jumps continually.

Materials and methods

A stock of 10X simHBS was prepared for the experiments. The final concentration of a 200 mL tested solution was 20 mM HEPES and 150 mM NaCl. The pH jump was initiated by the addition of either 200, 400, or 600 µL of respectively 12 M, 6 M, and 4 M of NaOH or HCl to obtain a change of 2.4 mmol in hydronium ion concentration. A magnetic stirrer mixed the simHBS during the jumps to ensure a quick homogeneous solution and a traditional pH electrode was used to confirm the jump. The optode reading used was the phase reading as the jump stayed in the linear range of the optode and the reading frequency was set to 5 secs. The jump time was evaluated at 80 and 90% of the total jump.

Results and discussion

The traditional electrode reached the 100% of the jump in roughly 15 to 25 seconds. The 80 and 90% jump could not be evaluated as there was no online data acquisition for the electrode. Visually the jump was almost immediate and can be considered that 80% of the jump is achieved in less than 5 seconds. The optode on the other hand presented a slightly longer delay before reaching 80% of the jump (table 2).

Table 2: pH optode jump speed results

Jump	[HCl] alternatively [NaOH]	µL	80% jump down time (pH drops to 6.5)	80% jump up time (pH rises to 7.5)
1-6	12 M	200	54 s	39 s
7-12	6 M	400	44 s	34 s
13-18	4 M	600	42 s	30 s
19-24	12 M	200	41 s	29 s
25-30	6 M	400	38 s	26 s
31-36	4 M	600	38 s	28 s

The systematic result, shown in the table, that a down jump is longer that an up jump, is due to the HEPES buffer. This tendency was also visible on the pH meter. Jumps 19 to 36 are a repeat of the first 18 jumps. Each jump lasting 4-5 min, the optode reached its fastest reaction time after being a minimum of 1 h 30 min in the simHBS with an 80% jump up reaction time under 30 s. This suggests that reading the optode at less than 30 s intervals is unnecessary. Especially with the drift [PreSens pH-1 manual pg. 9] due to bleaching by the laser source.

pH optode in a CHO suspension culture

Objective

To establish if the pH optode system is applicable in animal cell cultures, a comparison was made with a traditional electrode in the same cell culture. PreSens with Corning are already marketing a gamma-sterilized disposable spinner flask with integrated optode sensor. As this is a new product, there is a lack of experience in problems that may have been overlooked when switching to this new technology. A culture using both an optode and a traditional electrode should show excellent correlation to validate the use of the optodes. This is also the first test for the optodes in mammalian cell culture on a shaker system. PreSens GmbH together with Kuhner AG, have recently started to commercialize a shaker platform with integrated pH and oxygen PreSens optode system.

Materials and methods

A 1 L glass spinner was adapted with a traditional electrode using the hole in the cap as the point of entry for the Mettler Toledo autoclavable pH electrode (fig. 33). Once the electrode was secure, it was calibrated at 37°C with buffers 4, 7 and 10. The spinner was autoclaved and under a laminar flow hood, the optode was stuck to the interior surface using silicone glue (assumed non-contaminated) and a disposable pipette. 800 ml of proCHO5 supplemented with 16 mL of 200mM Glutamine and HT (hypoxanthine and thymidine) were filled into the spinner with 8 ml penstrep antibiotics. The spinner was left overnight in the shaker with the pH traditional electrode meter (pH meter 340) connected to an analogic paperfeed recorder (Rec 111) and the optode pH-1 mini set at 30 s intervals. Inoculation was done at $1x10^6$ CHO DG44 (passage 25) cells per millilitre.

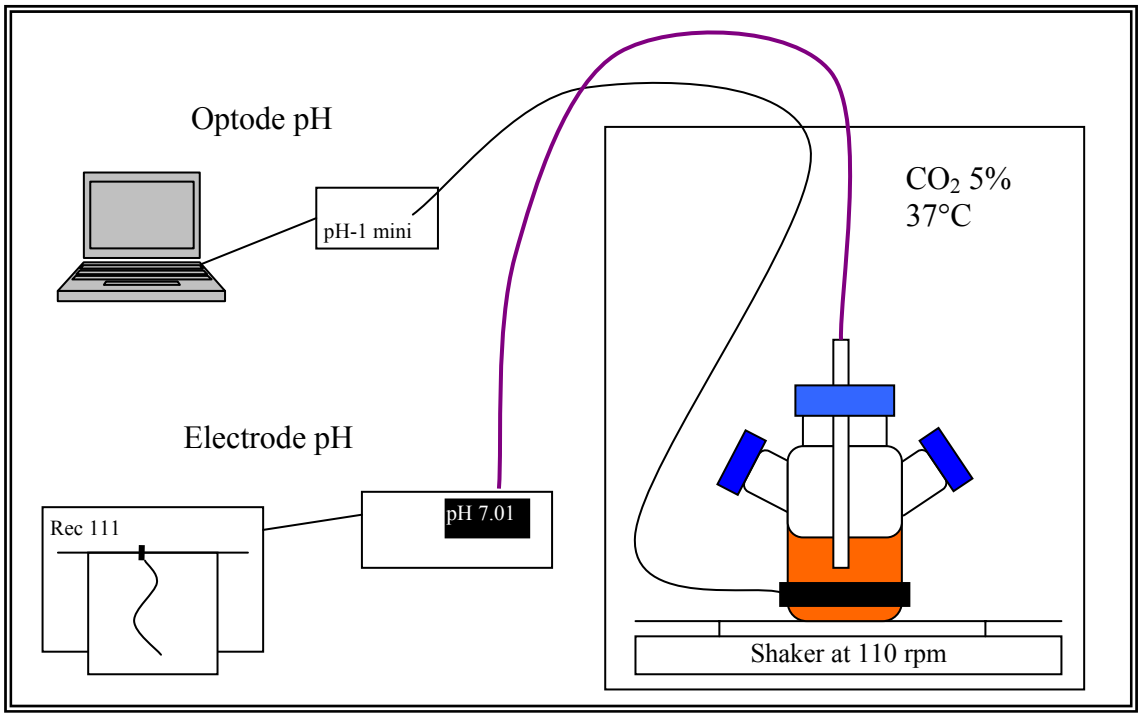

Figure 33: Spinner with optode and electrode for pH online measurement setup

Results and discussion

The culture was followed (fig. 36) just over thirteen days with the cells reaching a concentration of at least 6,5x10e6 ¢/mL between day 4 and 5. The cells begin their death phase from day 6 after having consumed all the glutamine and glucose in the media and die off slowly within 5 days. The pH reading from the traditional online electrode shows an immediate decrease of the pH from 7.5 to 6.8 within two days. The HEPES buffer used in the

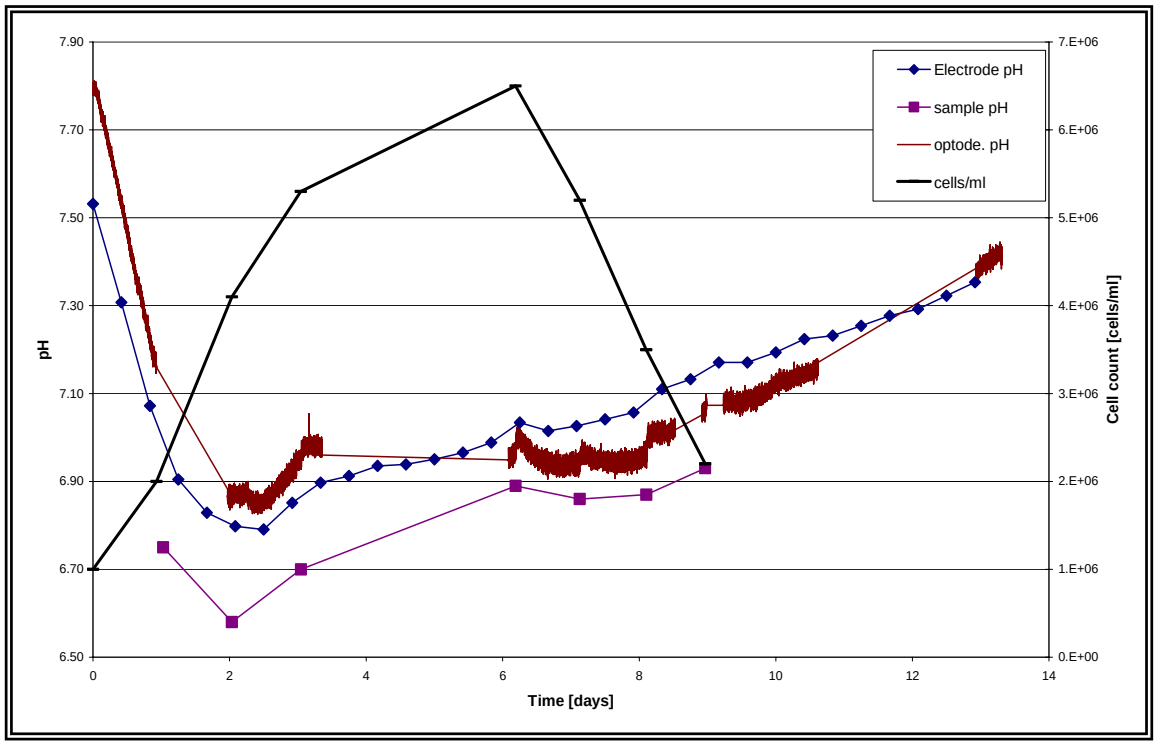

Figure 36: Electrode, Optode and offline pH values with cell growth curve

cell media is linear from around a pH of 6.5 to a pH of 8.5 as per the figure (fig 35) here below. The CO_2-bicarbonate buffer obtained with the partial pressure of CO_2 maintained at 5% in the shaker cabinet will push the pH towards 7.5 as can be seen by the first value (after a day in the shaker –for checking the sterility) of the pH traditional electrode. As the cell concentration stabilizes, the pH can now gently rise back to 7.5 as the glutamine having been used up does not get converted to more lactic acid.

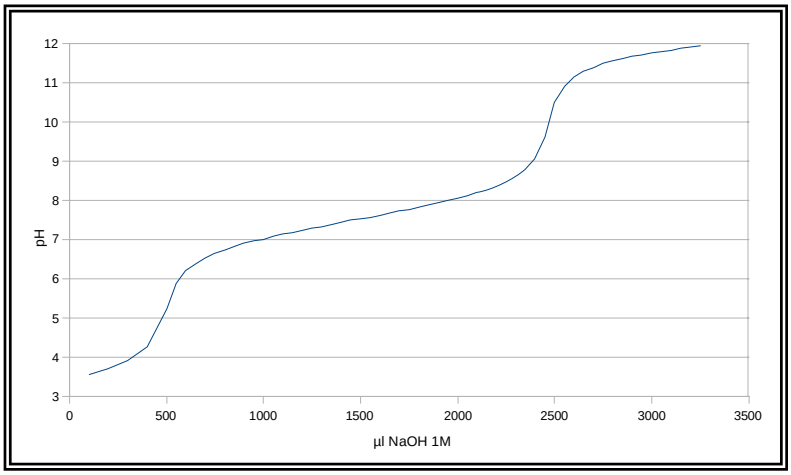

Figure 35: HEPES titration graph linear between pH 6.5 and 8.5

The offline measurement poses a few calibration problems. Even though, it closely follows the pH change pattern of the online pH electrode. The offline measurements were made after filling a 15ml tube with a 5ml sample. The offline electrode was calibrated before it was dipped into the sample and mixed with a pumping movement until a stable value was noted. The stability of the value was automatically done by the electronics of the pH meter using the autoread function. Temperature was also recorded and a more than 10°C difference was systematically observed within the 5 minutes of measuring the sample with the offline pH meter. A serious degassing effect of a pH offset of 0.2 appears to be the result of this sampling technique while waiting for the autoread function to take the reading. The temperature effect according to literature [wiki and fluka website] only affects the pH by about three hundredths which is a log fold difference to the results seen in the graph. The offline measurement has a built-in temperature sensor near the sensor tip.

Additionally to the sampling for pH offline measurement and cell counting, a 1.5 mL tube was filled to the absolute maximum level and tightly shut after which it was immediately stored at -20°C. These samples were then tested all together, after the end of the culture, on a NOVA BioProfile 200 analyser for the pH, glutamine, glutamate, lactate, glucose, bicarbonate ion, partial pressure of oxygen and of carbon dioxide. These information are treated in the following three graphs (fig. 37, 38, 39) keeping the offline pH measurement as well as the cell count as a reference on each graph.

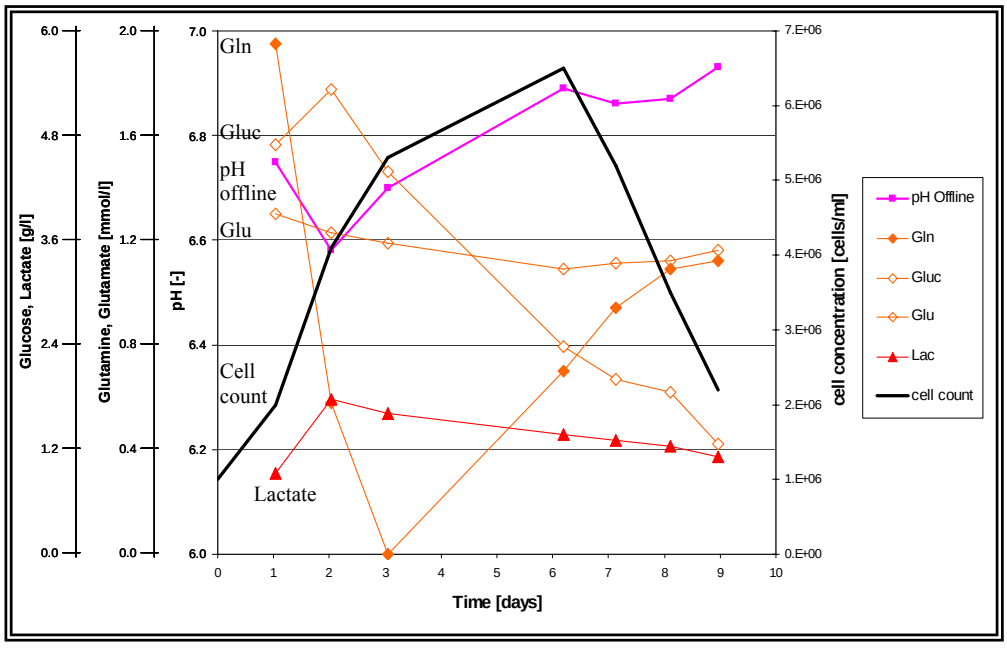

Figure 37: Glutamine (Gln), glucose (Gluc), glutamate (Glu), lactate (Lac) evolution over 9 days

The glutamine falls quite rapidely and is completely depleted even before the cells reach their maximum density. A signal then appears, but this could be bye products of dying cells. As a response to the glutamine decrease the lactate value increases but it then has a decreasing trend almost inversely proportional to the increasing pH value. The glucose appears to act like a secondary substrate and decreases more once the glutamine is used up. The glutamate is pretty stable, but has a slight increasing trend again in the dying part of the culture.

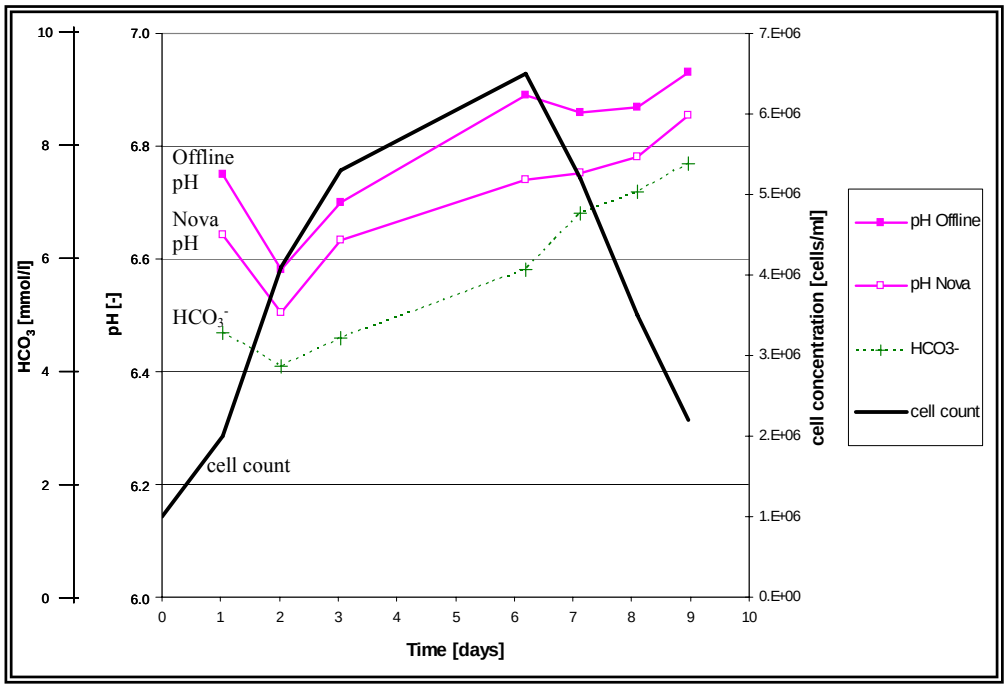

Figure 39: pH values of the different methods used and a comparison with the bicarbonate ion

The samples were frozen and stored for about a month before they could be analysed. This analysis shows another down shifting of about 0.1 pH compared to the offline values. The calibration of the Offline pH electrode definitely posed a problem The only affirmation which can be stated is that the trend or pH evolution is the same for each of the three other graphs. Below (fig. 37), the gas graphs don't have any particular modification and stay stable. This may indicate that there is enough gas transfer through the slightly unscrewed spinner lids.

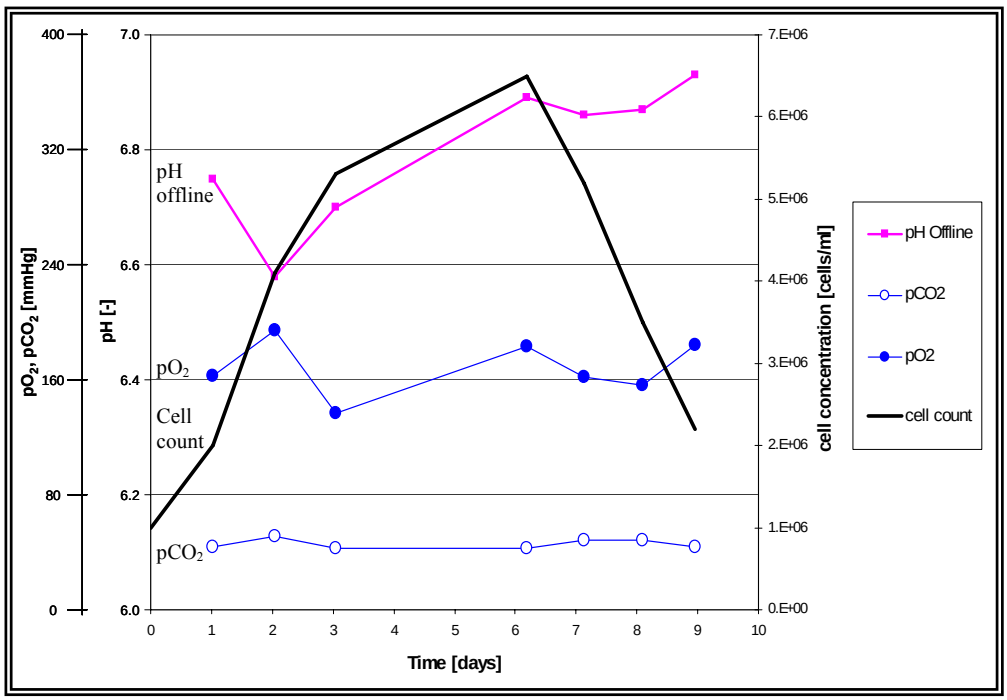

Figure 38: Oxygen and carbon dioxide pressures

Chapter 3:

Computational fluid dynamics

Introduction

Having observed a lot of phenomena in the practical analysis of a liquid in a shaking vessel, it is also necessary to see if a theoretical model can be made. Using the principal that each point in a fluid is affected by its properties and by its neighbours, it is possible to calculate what will happen to this point at any given point of time. The ideal point would be an atom, and calculating the effect of each atom on one another would be possible, but the number of atoms in a visible quantity of liquid is still far too high to run simulations in a reasonable time frame. Simplifications are needed by grouping similar regions that will act as one point. The optimal simplification depends on the precision needed in the result. Computational fluid dynamics allows the use of equations that may not have theoretical solutions, as is explained in the following quote. *"The Navier-Stokes equations are also of great interest in a purely mathematical sense. Somewhat surprisingly, given their wide range of practical uses, mathematicians have yet to prove that in three dimensions solutions always exist (existence), or that if they do exist they do not contain any infinities, singularities or discontinuities (smoothness). These are called the Navier-Stokes existence and smoothness problems. The Clay Mathematics Institute has called this one of the seven most important open problems in mathematics, and offered a $1,000,000 prize for a solution or a counter-example."*[Wiki Navier-Stokes]. The definition of the problem, by the Clay Mathematics Institute, is shown in appendix XXX.

The points described here above are associated to nodes of a mesh. The mesh is the basis on which the algorithms are used. The number of nodes of the mesh determines the number of calculations that need to be done. Supercomputers are used to do all the calculations which have massively parallel processors to do more calculations in the least amount of time. In our case, the number of nodes was close to a million, and the time necessary to reach a result for 60 seconds of simulation is approximately a fortnight. The long time needed to run the simulation also depends on the time interval used, in this case 0,001s. The model worked

upon is the 28cm Plexiglas® cylinder described in Materials and Methods. The liquid simulated is water and the programming done on FLUENT 6.3 (developed by Fluent Inc).

The work for the fluid dynamic model and simulation was done by Dario De Sanctis and Marco Perrone for their master in mathematics. In the following pages, a presentation of their results, with comments, is made. One must bear in mind that this is a simulation. A simulation only gives a theoretical value or answer. Any simulation must still be validated with different techniques. The more correlations between the theoretical simulation and the reality, the more one may consider the simulation as a true representation of what is really happening.

The VOF

The volume of fluid model is used to define the interface (fig. 40) between the water and the air. It is a convenient and powerful tool for modelling fluid flows which contain a free surface [Nichols et al., 1980]. This is necessary as the nodes of the mesh cannot be associated to only

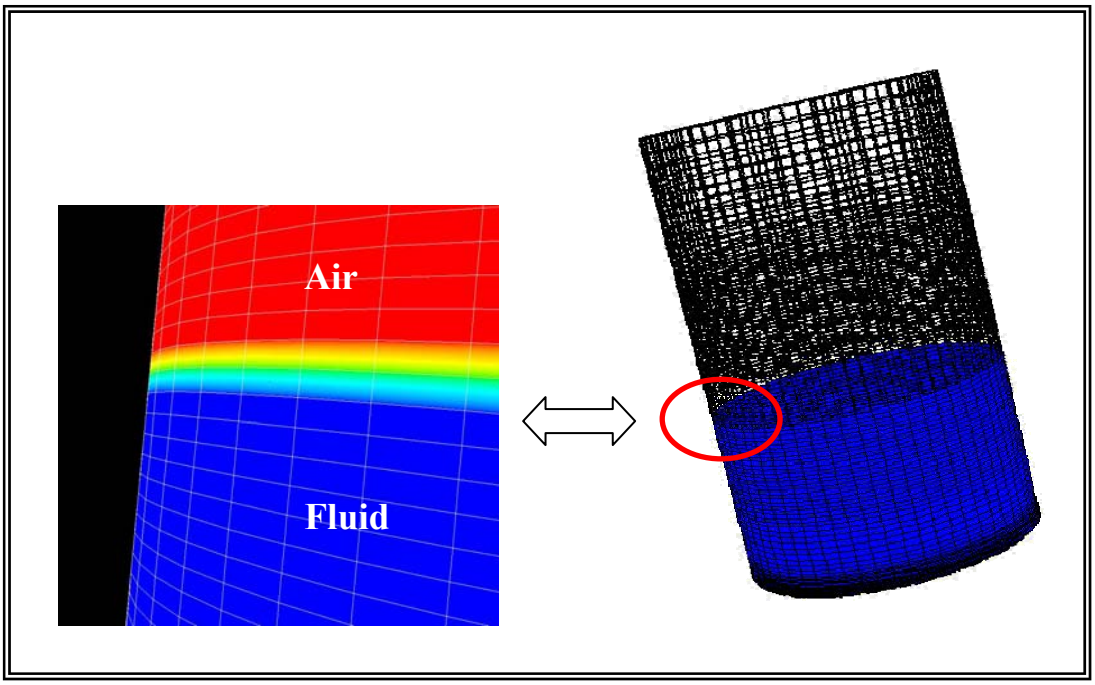

Figure 40 Visualisation of Interface

water or air because of the movement of the liquid. In other words, it is the value of the node that changes and not its position. In numerical fluid simulations, where the VOF function is averaged over each computational cell, the function becomes one in cells containing only fluid, zero in cells containing no fluid, and between these values in cells which contain a free surface [Harvie et al., 2000].The fluid is treated as an incompressible fluid and this means that the following equations (fig 41) are defined.

$$\alpha_{air} = \frac{V_{air}}{V_{tot}} \qquad \alpha_{fluid} = \frac{V_{fluid}}{V_{tot}}$$

$$\alpha_{air} + \alpha_{fluid} = 1$$

Figure 41: Volume of Fluid equations

The Mesh

It is the basis of all the calculations. Every node in the mesh (fig 42) will help determine what is happening. The more nodes, the more precision will be gained in the end result. It is interesting to note that higher concentrations of nodes are seen on the middle and lower region of the cylinder. This is merely to reduce the number of calculations that need to be done. The information wanted is the movement of the liquid and not the movement of the air. Thus more nodes are defined where the liquid moves the most and the least nodes are in the region where only air movement is possible. This information is taken from the practical observations and a security margin is added just in case. Here, there are about 700'000 nodes.

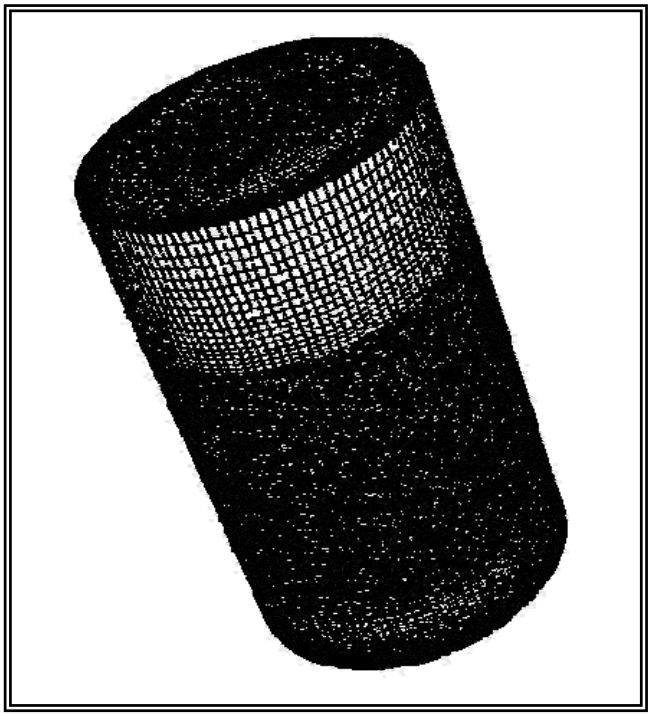

Figure 42: Grid of 700'000 nodes used for the simulation of the 28cm diameter vessel

Observing the water fraction with this mesh yields the following image (fig. 43). This is also the image at time zero. All the points have a zero velocity vector. Red is the fluid and the interface is the transition to blue.

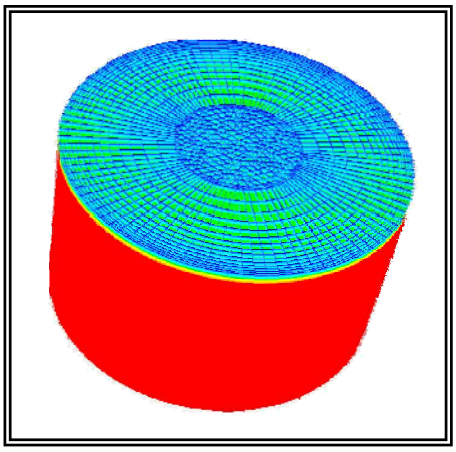

Figure 43: Water fraction at time 0, all points are at rest

Different observations of the simulation

Once the simulation is finished, it is possible to view the results depending on what was recorded at each point of time. The fluid position (fig. 44) is the most visible aspect of this simulation. This gives a volumetric representation of what is happening, but a closer look into what the liquid is doing is necessary. The main theme is mixing and knowing the flow of the liquid will help in understanding this. Thus a velocity flow diagram (fig. 45) will show the speed and direction of the fluid at every node.

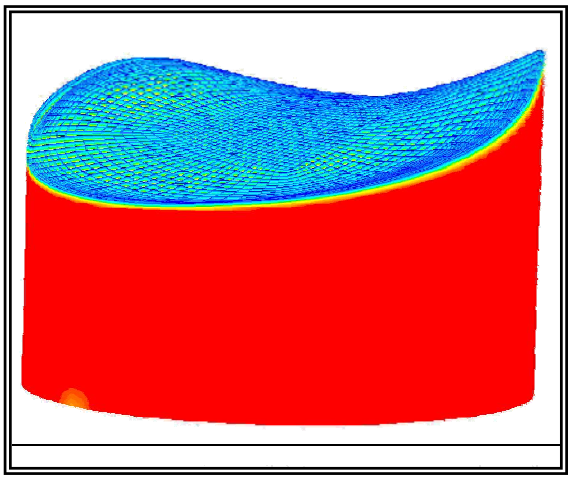

Figure 44: Fluid shape after 15 seconds of simulation

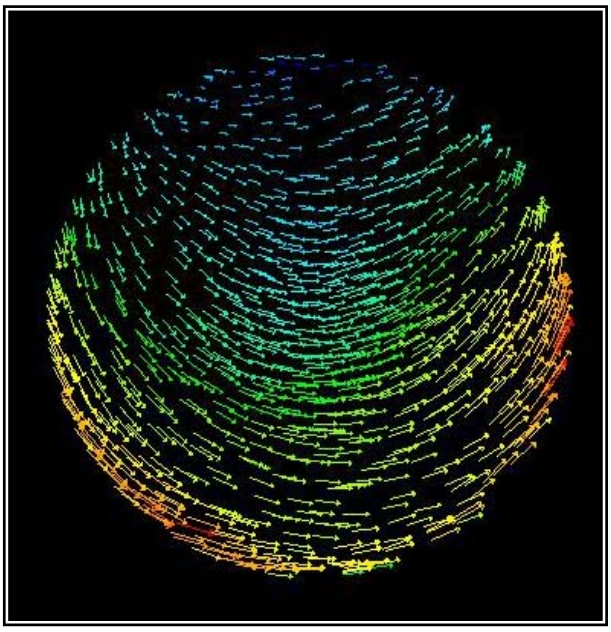

Figure 45: Top view of surface velocity vectors

Possibly the most interesting representation of what is happening inside the fluid is the velocity field (fig. 46 and fig. 47) in a plane normal to the base.

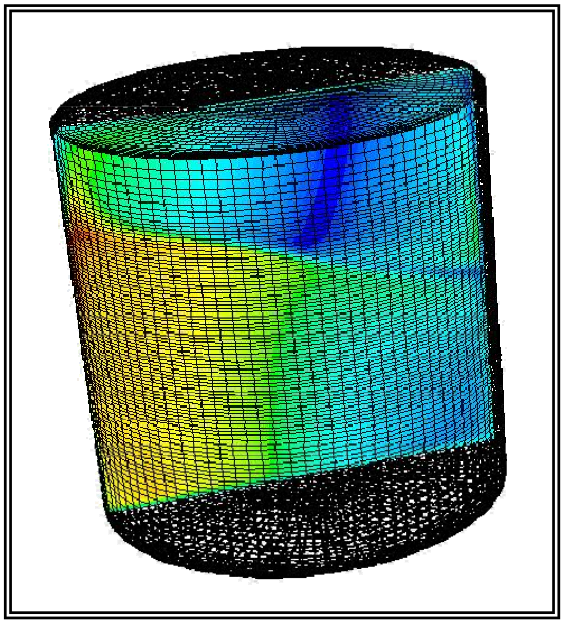

Figure 46: Velocity field plane normal to the base

Red is the higher velocities and blue the lowest. The interest lies in the difference between the air speed and the liquid speed. As air is compressible and far more fluid as compared to water, it is potentially at a different speed to the water at every point of the surface. This could be compared to a breeze of wind. A breeze implies a flow and thus as mixing of the air. It is then possible to hypothesize that the gas transfer to the liquid is increased due to the interface not having a gas deprived region. Viewing this diagram, it is clear that the air also has the highest velocities near the sides of the vessel due to the displacement of the liquid. High movement of the liquid is under the crest of the "wave" and lowest velocities are in the lull.

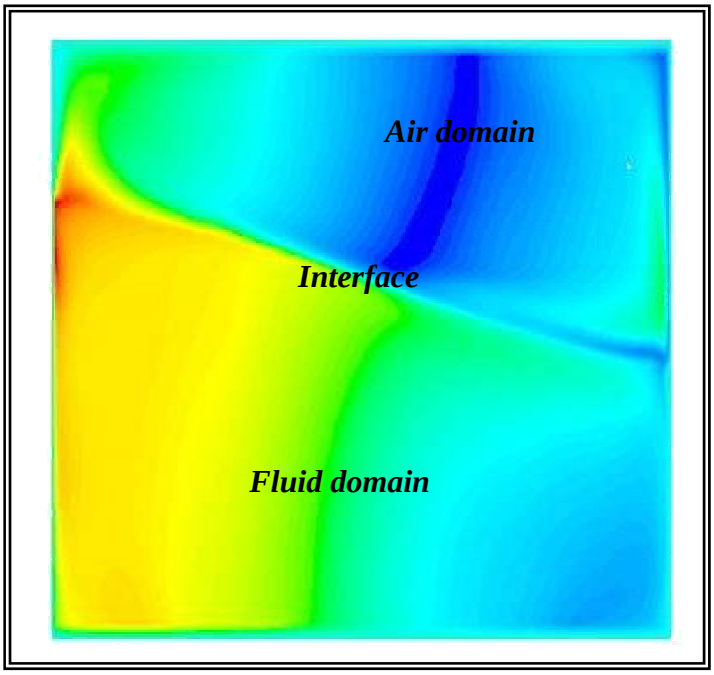

Figure 47: Velocity plane cleared of the mesh

Shear stress can be represented by asking the simulation to calculate and record the pressure at each node. As shear stress mainly occurs because of friction with the surface of the vessel, it is efficient to show the representation with isobars (fig. 48) on the vessel's surface. The highest pressure is on the front part of the double wave. This is logically correct due to the liquid being forced up the vessel surface. The second high pressure gradient is at the lowest point and this can be explained by saying that the liquid has just come down from the wave and has "hit" the bottom level. A change in direction implies quite high pressure.

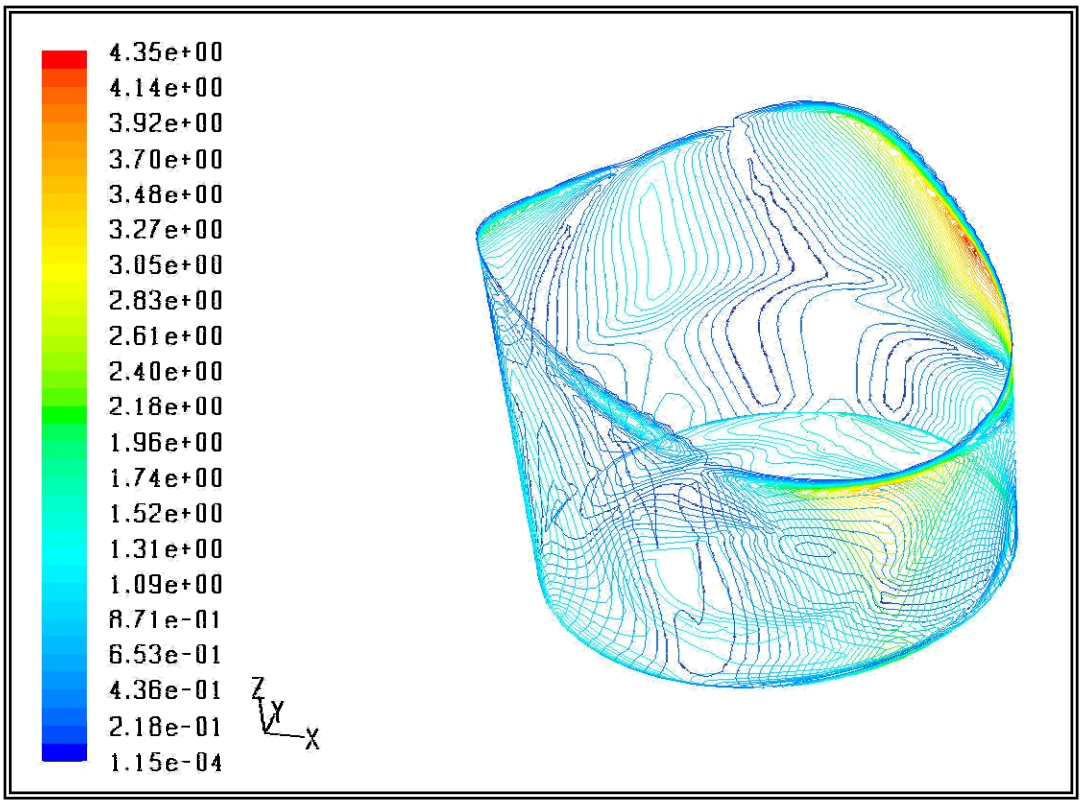

Figure 49: Contours of wall shear stress in Pa at 15 seconds

The next step in the simulation is with other meshes. The TubeSpin® or CultiFlask 50 (fig. 50) is being used as a high throughput minibioreactors [DeJesus et al., 2004], but nothing has been published about the flow patterns in these vessels. A newly developed helical track system (fig. 49) to increase gas exchange would benefit from a simulation by showing the shear stress values and integrating a gas diffusion model would prove the advantage of the helical track.

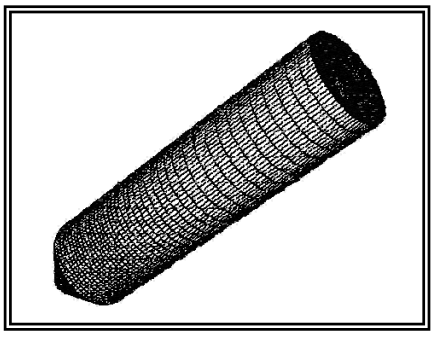

Figure 48: TubeSpin mesh

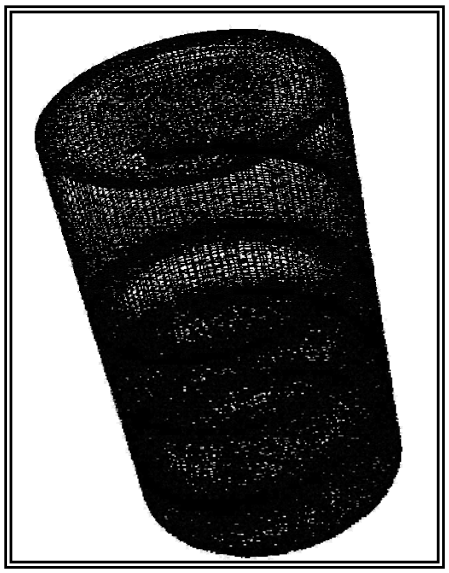

Figure 50: Helical track inside the 28cm cylinder

The dissolved oxygen model

The dissolved oxygen model is still only in 2D and is based on the diffusion law (Fick II). Figure 51 shows the law and its solution for a 2D model with a single surface (top) considered as always being at air saturated water which corresponds to an oxygen concentration of 6.9mg/l at 35.4°C. This value is from the table in the Oxygen optode manual [PreSens Oxy 4 Manual appendix pg. 55].

Fick II

$$\frac{\partial C}{\partial t} = D\frac{\partial^2 C}{\partial x^2}$$

Solution

$$\frac{C}{C_{SAT}} = 1 - \frac{4}{\pi}\sum_{n=0}^{\infty}\frac{(-1)^n}{2n+1}\exp\left[-\frac{D(2n+1)^2\pi^2 t}{4L^2}\right]\cdot\cos\left[\frac{(2n+1)\pi x}{2L}\right]$$

Figure 51: Fick's law of diffusion and its mathematical 2D solution

The visual effect of simple diffusion can clearly be seen in the image (fig. 52) along side at three different times.In comparison to the theoretical solution of the 2D diffusion law, the simulated model closely follows the graph and can be considered as a good model. The theoretical solution graph was calculated with Maple using the solution (fig. 53) equation and the simulation was run on Fluent using only the diffusion law.

This good correlation of the two graphs supports the use of the diffusion law as an applicable model and leads to believe that is would work in the three dimensional model.

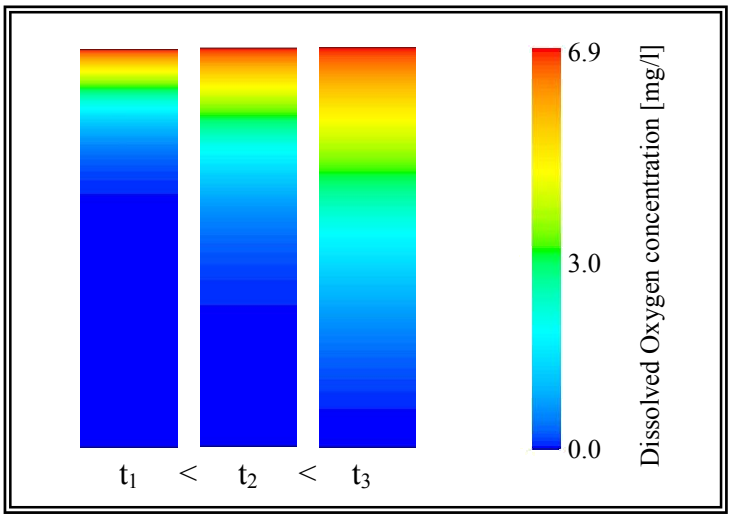

Figure 52: Diffusion of oxygen at three different time points

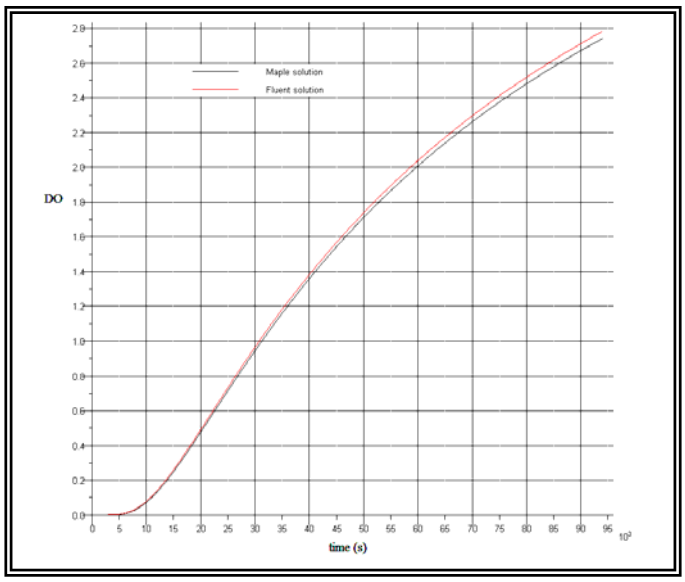

Figure 53: Theoretical (Maple) and simulation (Fluent) curve are a good match

Conclusion

Computational fluid dynamics is an extremely powerful tool when the model is proven similar to the reality. This proof is the most complicated part of the work. At the moment, the simulation visually corresponds to the reality as can be seen in the comparison image (fig. 54) here below. Further work is needed in this study and only collaborations with other scientific domains - such as image analysis, velocity field laser analysis, high speed photography, aerodynamics, rheology etc – will bring the proof that the model is a valid model.

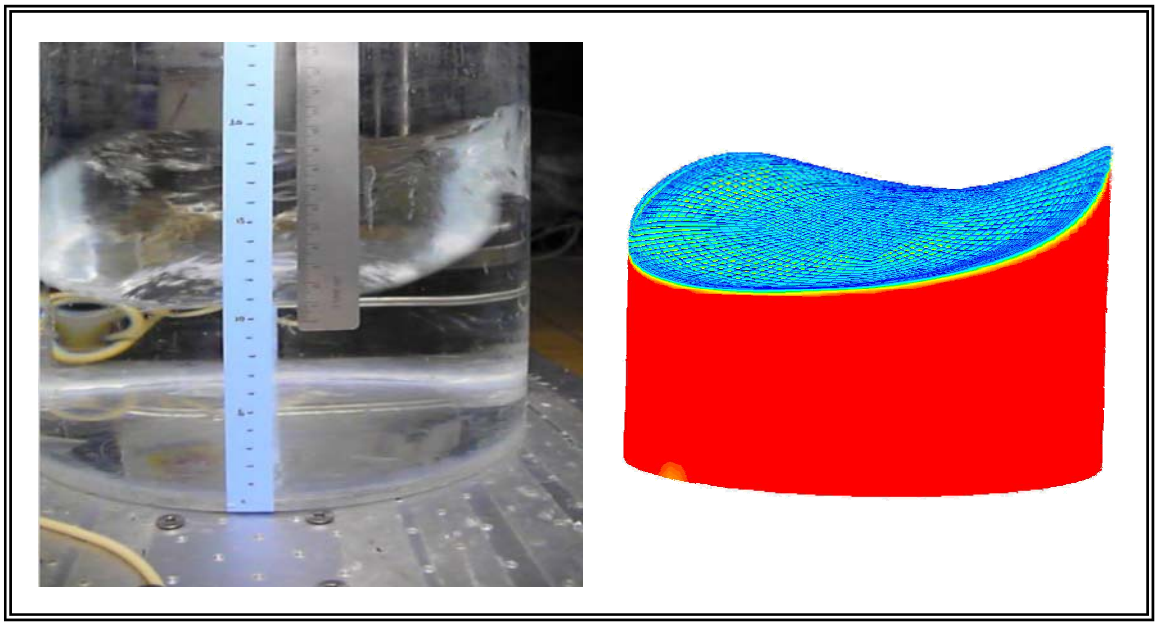

Figure 54: Comparison between reality and simulation

General discussion

The results presented in this report all show that orbital shaking bioreactors have a lot of interesting phenomena to exploit in cell cultivation. The mixing analysis study using a camera shows that simple techniques exist and that apparently strange movements can be isolated, and represented in a mathematical form. The double wave formula was found due to changing from a fixed referential (a person looking at the shaker) to a circular translation on a plane. Although the camera does distort the real distances, the resulting graphs are representative of the reality. There are many ways to get better results, but the infrastructure needs to be changed and this has a cost.

The Optode systems (developed by PreSens or Fluorometrics) are clearly the future in online monitoring of cell cultures. The sterility will be highly efficient through gamma sterilisation of the disposable bioreactor systems. The isolation of the product from exterior contaminations, due to previously sampling methods, will drastically fall. One must be conscious of the functionality of the optodes and always take into account this aspect when deciding on a new or traditional system. The optodes may be slow (compared to traditional electrodes) at reacting to a change, but cell cultures don't present jumps and drops of parameters in under the minute range. The Optodes are continually in the cell culture and 10 or 30 minute intervals will be sufficient for using optodes as the input for regulation systems.

Computational fluid dynamics must never be considered reality, but only an indication of what is most probably to happen. The ideal CFD would be a complete culture behaviour prediction but this will demand incredible calculating times. The result is also specific to the initial parameters, and a change in one of them means running the simulation once more. CFD is definitely a helping hand in bioreactor understandings but must be continuously validated with practical results

Conclusion

Although no data presented in this report can quantify the mixing efficiency in orbital shaken cylindrical vessels, the biotech industry can continue to use this cultivation technique and work through trial and error to obtain performing parameters. The study must go on and through the work done at using cameras and image analysis in this report, more mathematical hypothesises will eventually be found and one may finally relate vessel diameter, shaking diameter and shaking speed to a mixing efficiency factor. The mixing efficiency factor will then be included in the simulation model and the oxygen replacement rate will be found.

I hope that with this work, future students will be able to advance in answering the 2 questions asked at the end of the introduction.

Bibliography

(alphabetical order)

Anderlei T. Zang W., Papspyrou M., Büchs J. (2004). Online respiration activity measurements (OTR, CTR, RQ) in shake flasks. Biochem Eng J. 17 pp 187-194.

Büchs J. (2001) Introduction to advantages and problems of shaken cultures, Biochemical Engineering Journal 7 pp. 91–98

De Jesus MJ, Girard P, Bourgeois M, Baumgartner G, Jacko B, Amstutz H, Wurm FM. 2004. TubeSpin satellites a fast track approach for process development with animal cells using shaking technology. Biochem. Eng J. 17:217-223.

Duetz W.A., Witholt B., (2004) Oxygen transfer by orbital shaking of square vessels and deepwell microtiter plates of various dimensions. Biochem Eng J. 17 pp 181-185.

Freyer A.F., König M., Künkel A. (2004). Validationg shaking flasks as representative screening systems. Biochem Eng J. 17 pp 169-173.

Haldankar R., Li D., Saremi Z., Baikalov C., Deshpande R. (2006). Serum-free suspension large-scale transient transfection of CHO cells in WAVE bioreactors. Mol Biotech, vol 34, pp. 191-199.

Harvie D. J. E., Fletcher D. F. (2000). The stream volume of fluid advection algorithm, ANZIAM J. 42 (E) pg C690-C711,

Klimant I., Huber Ch., Liebsch G., Neurauter G., Stangelmayer A., Wolfbeis O.S. (2001). Dual Lifetime Referencing (DLR) - a New Scheme for Converting Fluorescence Intensity into a Frequency-Domain or Time-Domain Information, in New Trends in Fluorescence Spectroscopy: Application to Chemical and Life Sciences, Valeur B. & Brochon J.C. (eds.) Springer Verlag, Berlin. chap. 13, 257-275.

Lotter S., Büchs J., (2004). Utilization of specific power input measurements for optimization of culture conditions in shaking flasks. Biochem Eng J. 17 pp 195-203.

Maier U., Losen M., Büchs J. (2004). Advances in understanding and modeling th gas-liquid mass transfer in shake flasks. Biochem Eng J. 17 pp 155-167.

Nichols B. D., Hirt C. W., Hotchkiss R. S. (1980). SOLA-VOF: A solution algorithm for transient fluid flow with multiple free boundaries. Technical Report LA-8355, Los Alamos Scientic Laboratory, August.

Peter C.P., Lotter S., Maier U., Büchs J. (2004). Impact of out-of-phase conditions on screening results in shaking flask experiments. Biochem Eng J. 17 pp 205-215.

PreSens GmbH, Huber, Krause (2004). Instruction Manual pH-1 mini fiber-optic phase detection device. PreSens Regensburg DE.

PreSens GmbH, John, Huber (2004). Instruction Manual Oxy-4 4-channel Fiber-Optic Oxygen Meter. PreSens Regensburg DE.